รายงานวิจัยฉบับสมบูรณ์

โครงการ Synthesis of novel magnetic materials and Fe-based superconductors

โดย ผู้ช่วยศาสตราจารย์กิตติวิทย์ มาแทน

มิถุนายน 2557

สัญญาเลขที่ MRG55800

รายงานวิจัยฉบับสมบูรณ์

โครงการ Synthesis of novel magnetic materials and Fe-based superconductors

ผู้ช่วยศาสตราจารย์กิตติวิทย์ มาแทน

ภาควิชาฟิสิกส์ คณะวิทยาศาสตร์ มหาวิทยาลัยมหิดล

สนับสนุนโดยสำนักงานคณะกรรมการการอุดมศึกษา

และสำนักงานกองทุนสนับสนุนการวิจัยและมหาวิทยาลัยมหิดล

Abstract

Project Code: MRG55800

Project Title: Synthesis of novel magnetic materials and Fe-based superconductors

Investigator: Kittiwit Matan, Faculty of Science, Mahidol University

Email address: kittiwit.mat@mahidol.ac.th

Project Period: 2 years

Neutron scattering was used to study two structurally similar compounds, $Rb_2Cu_3SnF_{12}$ and $Cs_2Cu_3SnF_{12}$. High-intensity pulsed neutron scattering reveals a new set of magnetic excitations in the pinwheel valence-bond solid (VBS) state of the distorted kagome lattice antiferromagnet $Rb_2Cu_3SnF_{12}$. The polarization of the dominant dispersive modes (2 meV < $\hbar\omega$ < 7 meV) is determined and found consistent with a dimer series expansion with strong Dzyaloshiskii-Moriya interactions (D/J = 0.18). A weakly dispersive mode near 5 meV and shifted “ghosts” of the main modes are attributed to the enlarged unit cell below a T=215 K structural transition. Continuum scattering between 8 meV and 10 meV might be interpreted as a remnant of the kagome spinon continuum.

While the ground state of $Rb_2Cu_3SnF_{12}$ is the VBS state, that of $Cs_2Cu_3SnF_{12}$ is a classical Néel state. Magnetic excitations in the spin-1/2 distorted kagome lattice antiferromagnet Cs_2Cu_3SnF12, which has an ordered ground state owing to the strong Dzyaloshinskii-Moriya interaction, were studied using inelastic neutron scattering. Although the spin-wave dispersion can be qualitatively understood in terms of linear spin-wave theory (LSWT), the excitation energies are renormalized by a factor of approximately 0.6 from those calculated by LSWT, almost irrespective of the momentum transfer. This inadequacy of LSWT, which is attributed to quantum fluctuations, provides evidence of negative quantum renormalization in the spin-1/2 kagome lattice antiferromagnet.

Keywords: strongly correlated electrons, neutron scattering, quantum spin state, spin-wave excitations

บทคัดย่อ

รหัสโครงการ: MRG55800

ชื่อโครงการ: Synthesis of novel magnetic materials and Fe-based superconductors

ชื่อนักวิจัย และสถาบัน: กิตติวิทย์ มาแทน คณะวิทยาศาสตร์ มหาวิทยาลัยมหิดล

Email address: kittiwit.mat@mahidol.ac.th

ระยะเวลาโครงการ: 2 ปี

สารประกอบสองชนิดที่มีโครงสร้างคล้ายกัน $Rb_2Cu_3SnF_{12}$ และ $Cs_2Cu_3SnF_{12}$ ได้ถูกนำมาศึกษาโดยการวัดการกระเจิงของนิวตรอน สารประกอบทั้งสองนี้มีโครงสร้างแบบ kagome คือมีการจัดเรียงของสามเหลี่ยมโดยมีมุมร่วมกัน จากการวัดการกระเจิงของนิวตรอนจากแหล่งกำเนิดที่มีความเข้มสูง ทำให้เห็นการกระตุ้นเชิงแม่เหล็กที่ไม่เคยวัดได้มาก่อน ในสถานะ pinwheel valence-bond solid (VBS) ของ $Rb_2Cu_3SnF_{12}$ การศึกษา polarization ของการกระตุ้นระหว่างพลังงาน 2 meV และ 7 meV พบว่าสอดคล้องกับการคำนวณโดยใช้ dimer series expansion ที่มีค่าของ Dzyaloshiskii-Moriya interactions สูง นอกจากนี้ยังพบว่าการกระตุ้นในช่วง 5 meV และ “ghost mode” ยังสามารถอธิบายได้พิจารณา unit cell ที่มีขนาดใหญ่ขึ้นเนื่องจากการเปลี่ยนเฟสที่อุณหภูมิ 215 K continuum scattering ระหว่าง 8 meV และ 10 meV อาจจะมีต้นกำเนิดมาจาก spinon continuum ซึ่งถูกค้นพบเมื่อไม่นานมานี้ในสารประกอบที่มีโครงสร้างแบบ kagome

ในขณะที่สถานะพลังงานต่ำสุดของ $Rb_2Cu_3SnF_{12}$ เป็น VBS สถานะพลังงานต่ำสุดของ $Cs_2Cu_3SnF_{12}$ เป็นแบบ classical Néel state การกระตุ้นเชิงแม่เหล็กของ $Cs_2Cu_3SnF_{12}$ ซึ่งเป็น spin-wave หรือ magnon ถูกศึกษาโดยใช้การกระเจิงของนิวตรอนแบบไม่ยืดหยุ่น จากผลการทดลอง ถึงแม้ว่า spin-wave dispersion จะอธิบายได้ด้วย linear spin-wave theory (LSWT) แต่ค่าของพลังงานในการกระตุ้นมีขนาดลดลงประมาณ 60% ซึ่งเกิดจาก quantum fluctuations ผลการทดลองนี้จึงเป็นหลักฐานชิ้นแรกที่แสดงให้เห็นถึง negative quantum renormalization ในสารประกอบ kagome

คำหลัก: strongly correlated electrons, neutron scattering, quantum spin state, spin-wave excitations

Introduction

Collective behavior of electron spins in a geometrically frustrated magnet could potentially give rise to a diversity of unconventional ground states including the most sought-after quantum spin liquid state. Geometric frustration is due to the incompatibility between spin interactions and the underlying crystal lattice [1]. In this project, we have studied magnetic properties of a kagome lattice antiferromagnet (shown in Figure 1), which is one of the most highly frustrated lattice in two dimensions. Several theoretical studies have been applied to study low-energy spin dynamics of this geometrically frustrated magnet, and diverse classes of novel spin states have been proposed including a gapless U(1)-Dirac-spin-liquid state, a gapped-spin-liquid state, and a valence bond solid (VBS) state [2-4]. The difference between the spin-liquid states, which can be collective called the resonance valance bond (RVB) state, and the VBS state is that, whereas the gapped RVB state has short-range dimer-dimer (singlet pair) correlations, the VBS state has long-range dimer-dimer correlations that break the translational symmetry of the proper kagome lattice. In order to probe these states in a real system, one needs to look for their distinct features in magnetic excitations by means of inelastic neutron scattering. While the spin dynamics of the RVB state is continuum spin-1/2 excitations, that of the VBS state is spin-1 singlet-to-triplet excitations.

Experimentally, the quest for these states in a realizaion of the kagome lattice antiferromagnet has been hindered by the rarity of model systems. In recent years, the field has been rejuvenated by the discoveries of the kagome lattice in herbertsmitthite [5,6] and distorted kagome lattice in volborthite [7, 8]. Nevertheless, the lack of samples in a single crystal form and the presence of non-magnetic impurities at the magnetic sites make the study of these systems difficult. As a result, the presence of the quantum spin states cannot be confirmed. In our recent work, which has been published in Nature Physics, we have studied a stoichiometrically pure, spin-1/2 deformed kagome lattice antiferromanget $Rb_2Cu_3SnF_{12}$ with full occupancy of Cu^{2+} ions at the kagome lattice sites [9]. Using inelastic neutron scattering, we found that the low-energy spin dynamics are dominated by singlet-to-triplet excitations, which directly confirms that the ground state of this distorted kagome system is the long-sought-after RVB state. This work reveals the first direct

evidence for the presence of the RVB state in the kagome lattice system, validating some of the theoretical prediction [10]. The dimers in this RVB state form a pinwheel configuration as shown in Figure 1. This pinwheel state is stabilized by spatially non-uniform exchange interactions among spins. The singlet dimers are formed between two spins bonded by the largest exchange interaction J_1. Our results also show that the antisymmetric Dzyaloshinskii-Moriya (DM) interaction plays a significant role in determining the ground state and its spin dynamics. We employed the dimer series expansion to analyze the data, and were able to obtain all relevant microscopic spin Hamiltonian paprameters.

In this previous study, magnetic excitations from the singlet ground state were probed using inelastic neutron scattering on a triple-axis spectrometer. These measurements revealed the pinwheel motif of dimers, and determined the relevant spin Hamiltonian parameters through a dimer series expansion up to eighth order. However, the detailed structure of the excitations could not be resolved due to lack of resolution and counting statistics. For this work, we report high intensity pulsed neutron scattering measurements on single crystalline $Rb_2Cu_3SnF_{12}$ using the Cold Neutron Chopper Spectrometer at the Spallation Neutron Source, Oak Ridge National Laboratory. A time-resolved, highly pixelated detector system that covers a large solid angle (14% of the unit sphere) enabled concurrent measurements over a much wider range of momentum and at higher resolution than previously. We confirm the splitting of the triplet associated with dimerization into a doublet and a singlet as a result of strongly anisotropic interactions, and are able to unambiguously determine the polarization of each mode. More importantly, we discover a new family of modes associated with the structural superlattice, and a continuum at high energy, which may be related to the spinon continuum recently detected in the undimerized kagome system, herbertsmithite [11].

At room temperature, $Rb_2Cu_3SnF_{12}$ has the hexagonal R-3 space group with lattice parameters a = 13.917(2) Å and c = 20.356(3) Å. At 215 K, it undergoes a first-order structural transition, doubling the in-plane lattice constant a. The resulting lattice distortion is small so to a first approximation we use the room temperature structure, where a two-dimensional unit cell comprises 12 Cu^{2+} spins (Fig. 1). The spin-1/2 Cu^{2+} ions form a distorted kagome plane and are surrounded by

a deformed octahedral environment of fluorine. The kagome planes are separated by nonmagnetic ions, which results in weak interlayer interactions. The distorted kagome lattice gives rise to four antiferromagnetic in-plane exchange interactions $J_1>J_2>J_3>J_4$. To lowest order, spins interacting through J_1 form singlets which are linked through the weaker interactions. Powder neutron diffraction shows no magnetic order down to 1.3 K. The low-temperature magnetic susceptibility indicates a non-magnetic, spin singlet ($S_{tot}=0$) ground state and mixing of the singlet and triplet ($S_{tot}=1$) excited states through the DM interactions (S_{tot} denotes the quantum number for the total spin of a single dimer).

In our second work, we have studies magnetic excitations in $Cs_2Cu_3SnF_{12}$, which shows the ordered ground state at low temperature in contrast to $Rb_2Cu_3SnF_{12}$. Ubiquitous magnetic excitations in conventional magnets with the Néel state are generally well described by LSWT. In low-dimensional quantum magnets, however, dominant quantum effects significantly modify the magnetic excitations. In particular, for an S=1/2 antiferromagnetic Heisenberg spin chain, the exact spinon excitation energies are larger than that calculated using LSWT by a factor of $\pi/2$, which was verified through an inelastic neutron scattering experiment on the spin-1/2 one-dimensional (1D) Heisenberg antiferromagnet $CuCl_2 \cdot 2(C_5D_5)$. This quantum enhancement of excitation energies is known as the quantum renormalization. In this work, we present the first evidence of the large negative renormalization of spin-wave energies with respect to the LSWT result in $Cs_2Cu_3SnF_{12}$. This observation provides a striking contrast to the well-known positive quantum renormalization of excitation energies in the S=1/2 antiferromagnetic Heisenberg spin chain, for which the renormalization factor is exactly $\pi/2$.

$Cs_2Cu_3SnF_{12}$ has a uniform kagome lattice at room temperature with the lattice parameters a=7.142(4) Å and c=20.381(14) Å. This compound undergoes a structural transition at T_s=185 K and magnetic ordering at T_N=20.0 K. The magnetic susceptibility exhibits a small anomaly at T_s and a large increase at T_N. The presence of superlattice reflections below T_s suggests the doubling of the in-plane lattice parameter, giving rise to a 2a x 2a enlarged unit cell. Above T_N, the magnetic susceptibility is in good agreement with the theoretical susceptibility

obtained from exact diagonalization for the 24-site kagome cluster. This suggests that the exchange network remains approximately uniform. Low-energy magnetic excitations in the spin-1/2 distorted KLAF $Cs_2Cu_3SnF_{12}$ can be described by the collective disturbance of the ordered moments. Although these magnetic excitations in the classical spin-5/2 KLAF $KFe_3(OH)_6(SO_4)_2$ are well described by LSWT, little is known about the quantum effect for the spin-1/2 case, where large quantum renormalization is expected to emerge. Here, we present the first evidence of the large negative renormalization of spin-wave energies with respect to the LSWT result in $Cs_2Cu_3SnF_{12}$. This observation provides a striking contrast to the well-known positive quantum renormalization of excitation energies in the S=1/2 antiferromagnetic Heisenberg spin chain, for which the renormalization factor is exactly $\pi/2$.

Understanding ground states and their spin dynamics in the frustrated magnets, in which the emerging phenomena are due to collective behavior of electron spins, could potentially lead to new insight in other related subjects, such as high-T_c superconductivity, in which it has long been suggested that both frustration and magnetism could play a role in giving rise to such a high transition temperature [12], and anomalous quantum Hall effect, in which the chirality of spins in a non-colinear arrangement has been suggested to give rise to the phenomenon [13]. More importantly, physics of spin interactions in the strongly correlated regime could promisingly pave the way for the future of a new kind of electronic devices, the so-called spintronics.

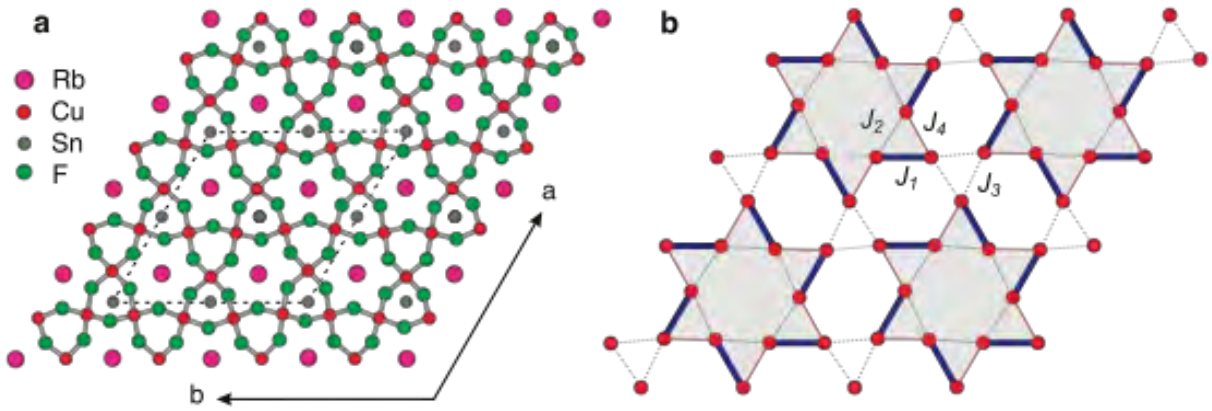

Figure 1 (a) A crystal structure of $Rb_2Cu_3SnF_{12}$ shows the connectivity of the Cu ions (red) forming a deformed kagome lattice. (b) The dimers shown in blue form the pinwheel VBS state. The exchange interactions are labeled as $J_1 > J_2 > J_3 > J_4$.

$Rb_2Cu_3SnF_{12}$

Experiments and Results

Single crystalline $Rb_2Cu_3SnF_{12}$ was synthesized from the melt. Inelastic neutron scattering measurements were performed on two co-aligned crystals with a total mass of 4 g and a mosaic of 1.5^o. The sample was mounted with the (H,0,L) reciprocal lattice plane horizontal to allow intensity integration of rod-like scattering along the L direction while taking advantage of the two dimensionality of the system. The incident energy E_i was fixed at 12 meV for an energy resolution (full width at half maximum) of 0.56(3 ~meV at the elastic position. The sample was cooled to a base temperature of 2 K using a He-4 cryostat. Multiple datasets were acquired by rotating the sample about the vertical axis, which is parallel to [-1,2,0], in steps of 2^o covering 68^o of sample orientation. An angle between the incident beam and [0,0,1] ranges from -28.5^o to 39.5^o. The background was measured at 70 K, where the excitations are very broad and weak. These datasets were subsequently combined to produce a background-subtracted, four-dimensional scattering-intensity function $I(\mathbf{Q},\omega)$, where $\mathbf{Q}$ is the momentum transfer and $\hbar\omega$ is the energy transfer. The data were sliced and cut along high-symmetry directions using MSLICE to produce contour maps, constant-$\mathbf{Q}$, and constant-energy plots.

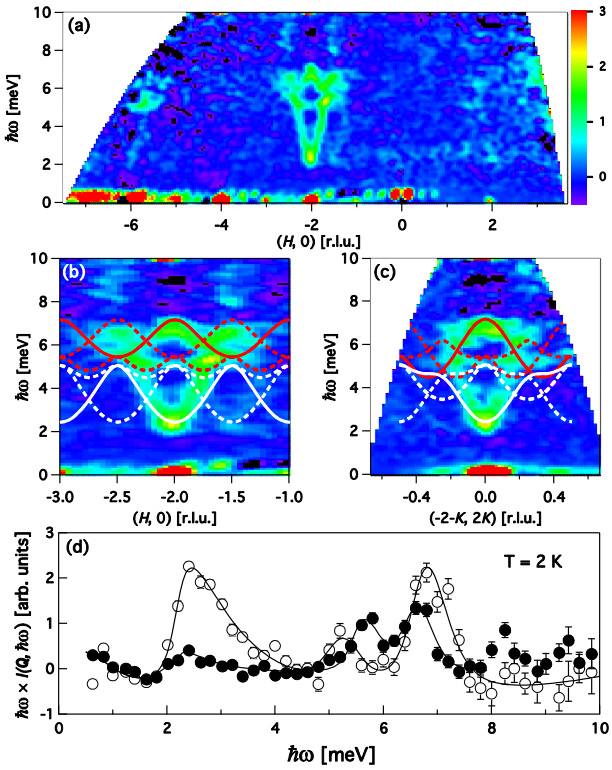

Figure 2 Contour maps show a product of scattering intensity and energy transfer $\omega \cdot I(\mathbf{Q}, \hbar\omega)$, displaying magnetic excitations in $Rb_2Cu_3SnF_{12}$ as a function of energy and in-plane momentum through (a), (b) (H, 0) and (c) (-2-K, 2K). The intensity is averaged over the available range of L, $\Delta\mathbf{Q}_{[1,0]}$ of 0.042 $Å^{-1}$, and $\Delta\mathbf{Q}_{[-1,2]}$ of 0.045 $Å^{-1}$. The measurements along [-K,2K] are limited by a smaller detector-coverage area perpendicular to the horizontal plane. Solid lines represent the excitations of the original spin Hamiltonian whereas dotted lines denote excitations resulting from the 2a x 2a enlarged unit cell. Red denotes the $S_{tot,z}$=0 mode and white denotes the $S_{tot,z}$=±1 mode. (d) Constant-**Q** cuts show $\hbar\omega \cdot I(\mathbf{Q}, \hbar\omega)$ at (-2,0) (open circles) and the average of $\hbar\omega \cdot I(\mathbf{Q}, \hbar\omega)$ at (-1.5,0) and (-2.5,0) (closed circles). Above 8 meV, the closed symbols lie above background, indicative of the continuum scattering. The lines are guides to the eye. The error bar represents one standard deviation.

A contour map of $\hbar\omega \cdot I(\mathbf{Q}, \hbar\omega)$ averaged over the L direction (the L-dependence of the scattering intensity will be discussed later), which is plotted as a function of energy and in-plane momentum along [H,0] (Fig. 2), shows a distinct pattern of excitations around (-2,0) and faint outlines of similar patterns displaced by ΔH=±4. The latter are barely detectable around the equivalent Brillouin-zone centers, (-6,0) and (2,0). The measurements were set up so integration along L is optimal at (-2,0). The difference in the intensity profile around (-2,0) and (2,0) is a result of a smaller range of intensity integration for the latter. The overall profile of the excitations around (-2,0) is consistent with our previous report. The lower branch, which has a broader band-width, is known to be a two-fold-degenerate excitation as it is split by a magnetic field along the c-direction. By mapping the L-dependence of the intensity of this branch, we shall later show that it is associated with transitions from the singlet ground state (S_{tot}=0) to a doublet with S_{tot}=1 and $S_{tot,z}$=±1 ($S_{tot,z}$ denotes the magnetic quantum number of the S_{tot}=1 triplet states). The upper branch, which has a smaller band-width, does not split in a field and so is thought to be a non-degenerate excitation from the singlet ground state to the singlet state with S_{tot}=1 and $S_{tot,z}$=0. We note that these states are not pure states of defined angular momentum due to the DM interactions.

A constant-**Q** cut at (-2,0) (Fig. 2(d)) shows clear resolution-limited peaks at $\hbar\omega$=2.4(3) meV and 6.9(3) meV, consistent with the previous data (where the uncertainty represents half the energy resolution). The contour maps around the zone center (-2,0) (Fig.~\ref{fig2}(b),~(c)) reveal a more intricate set of excitations than previously appreciated. A weakly dispersive mode around 5 meV is visible along both [H,0] and [-K,2K] (Fig. 2(b),(c)). At the zone center this mode peaks at 5.3(3) meV (Fig. 2(d)). It grows slightly more intense away from the zone center, which contrasts with the other two modes that become weaker. We also observe excitations centered around (-1.5,0) and (-2.5,0) (Figs. 2(b) and (a) (2.0-2.5 meV)), which resemble the mode around (-2,0) but with much less intensity, and hence are named the “ghost” modes. We have previously reported these ghost modes and attributed them to the enlarged unit cell caused by the structural transition. Our dimer series expansion shown by solid lines in Fig. 2(b),(c) and the bond-operator mean-field

theory cannot account for all of this observed scattering intensity between 2 meV and 7 meV as neither calculation considers the enlarged unit cell. Furthermore, we observe diffuse scattering between 8 meV and 10 meV near (-1.5,0) and (-2.5,0), which cannot be accounted for by the dimer series expansion.

Discussion

In this section, we first analyze the excitation dispersions of $Rb_2Cu_3SnF_{12}$ below 8 meV using the extended version of the dimer series expansion to include the effect of the enlarge unit cell. We then investigate the L-dependence of the intensity to determine the polarization of each mode. We end this section with a discussion of the diffuse scattering between 8 meV and 10 meV.

To understand the 5 meV mode and the ghost modes around (-1.5,0) and (-2.5,0), we consider the 2a x 2a enlarged unit cell consisting of 48 spins. We write the spin Hamiltonian as H + H', where H' represents a perturbation due to the enlarged unit cell. H' has the exact same form as H but the sum is over 48 spins in the enlarged unit cell. We then perform the dimer series expansion on the pinwheel VBS state using the Hamiltonian H + H'. The linked cluster expansion algorithm was used to generate a graphical series of dimers. The low-energy spectra are calculated up to eighth order in the inter-dimer and DM interactions using the Dlog-Padé approximation. We define the path $\Gamma \rightarrow \mathrm{M} \rightarrow \mathrm{K} \rightarrow \Gamma$ in the first Brillouin zone of the original model H.

It is interesting to note that the weakly dispersive mode in Fig. 2(b) is originally the excitation on the path between two adjacent M points. From the experiment, this mode is not symmetric around H = -1.75; its energy increases monotonically as H varies from -2 to -1.5. This suggests that we observe the $S_{tot,z} = \pm 1$ triplet excitations around the zone center, H = -2, and the $S_{tot,z} = 0$ triplet excitations away from there, which may be experimentally verified by measurements in a magnetic field. We note that the in-plane component of the DM vector d_p is set to zero in our dimer series expansion. A recent ^{63,65}Cu NMR study in high fields up to 30 T and neutron

scattering measurements show that the mixing between the singlet and triplet states via the DM interactions gives rise to a large residual gap. The anti-crossing of the singlet and triplet mode, which is due to the combined effect of the off-diagonal g-tensor and small d_p ($|d_p|$<0.012), prevents the gap from closing at high magnetic fields. However, d_p has little effect on the overall zero-field spectrum.

The scattering intensity displayed thus far was averaged over the L direction. However, the L-dependence of the scattering intensity contains valuable information about the polarization of the excitations and inter-plane correlations. Within the resolution of our measurements, there is no dispersion along L (Fig. 3(a)), which attests to the two-dimensional nature of the system. Contour maps of the scattering intensity integrated over the energy ranges $\hbar\omega$=[2.0,3.0] meV (Fig. 3(b)) and $\hbar\omega$=[6.5,7.5] meV (Fig. 3(c)) plotted as a function of H and L show rods of scattering that extend along L at H=-6, -2, and 2. The integrated intensity of the $S_{tot,z}$=±1 mode has broad maxima at L=3 and 6 before falling off at large L (Fig. 3(d)), while that of the $S_{tot,z}$=0 mode monotonically decreases as a function of L with a small hump around L=6 (Fig. 3(e)). The overall trend of the curves reflects the different polarization of the modes while the modulation of scattering intensity results from inter-plane correlations.

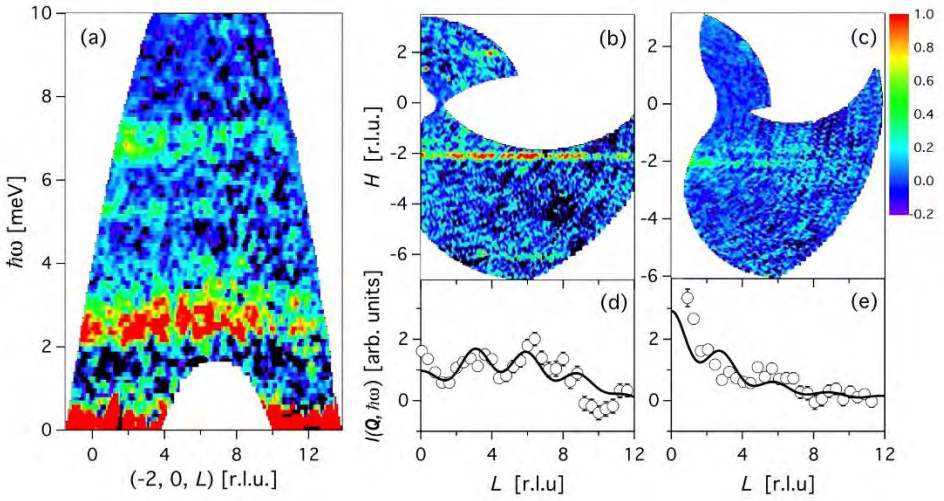

Figure 3. (a) Contour maps of I($\mathbf{Q}$,$\hbar\omega$) are plotted as a function of $\hbar\omega$ and L. The intensity is averaged over $\Delta\mathbf{Q}_{[1,0]}$ of 0.042 Å^{-1} and $\Delta\mathbf{Q}_{[-1,2]}$ of 0.045 Å^{-1}. The broadening is a result of the

integration along the in-plane momenta. (b) and (c) show contour maps of I(**Q**,$\hbar\omega$) plotted as a function of H and L. The intensity is energy-integrated for (b) $\hbar\omega$=[2.0,3.0] meV and (c) $\hbar\omega$=[6.5,7.5] meV. (d) and (e) show the L-dependence of I(**Q**, $\hbar\omega$) for energy ranges (d) $\hbar\omega$=[1.0,4.0] meV and (e) $\hbar\omega$=[6.0,8.0] meV centered at (-2,0). The intensity is averaged over $\Delta\mathbf{Q}_{[1,0]}$ of 0.10 Å^{-1} and $\Delta\mathbf{Q}_{[-1,2]}$ of 0.18 Å^{-1}. Solid lines denote the product of the magnetic form factor for Cu^{2+} spins, the inter-plane correlation function, and the polarization factor, assuming that modes are polarized (d) in the kagome plane and (e) out of the plane.

For the magnetic excitations in $Rb_2Cu_3SnF_{12}$, the polarization factor becomes $1\pm(Q_L/|\mathbf{Q}|)^2$, where Q_L is a component of **Q** along L. It grows (shrinks) with increasing L if the polarization is in-plane or transverse (out-of-plane or longitudinal). The inter-plane correlations, which are embedded in the dynamic structure factor, can be described by a function \$1+αcos(2πL/3), when the correlations along c only extend to the nearest neighbor plane located at c/3. Here the fit parameter, α, indicates the type and strength of inter-plane correlations. (Ferromagnetic for positive \$\alpha\$. Antiferromagnetic for negative α.) The product of the magnetic form factor for Cu^{2+} spins, which decreases monotonically with increasing L, the polarization factor, and the inter-plane correlation function denoted is in accordance with the in-plane (out-of-plane) polarization of the $S_{tot,z}$=±1 ($S_{tot,z}$=0) mode. Ferromagnetic inter-plane correlations are indicated by positive α (α=0.31(15)). The polarization analysis for the excitations around 5 meV close to the zone boundary, which is not shown, reveals mixing of the in-plane and out-of plane polarizations, or in other words the $S_{tot\}z}$=0 and $S_{tot,z}$=±1 modes merge near the zone boundary.

The magnetic excitation spectrum between 2 meV and 7meV in $Rb_2Cu_3SnF_{12}$ is markedly different from the spin-wave excitations observed in the classical spin-5/2 kagome lattice antiferromagnet $KFe_3(OH)_6(SO_4)_2$ (jarosite), which orders magnetically at low temperatures. It also differs from the continuum of spinon excitations in herbertsmithite, where the ground state is believed to be a quantum spin liquid. Resonant modes in $Rb_2Cu_3SnF_{12}$ are found only around the zone center and their intensity decreases precipitously away from (-2,0), while in jarosite the "weathervane" mode exists throughout the Brillouin zone and in herbertsmithite the spinon

continuum gives rise to hexagonal rings of diffuse scattering, surrounding zone centers. However, between 8 meV and 10 meV we observe for $Rb_2Cu_3SnF_{12}$ weak diffuse scattering near (-1.5, 0) and (-2.5, 0) on both sides of the zone center (-2,0), as in herbertsmithite. This scattering, which is diffuse in energy and broad in momentum, is different from the resolution-limited excitations below 8 meV and cannot be accounted for within the dimer series expansion. For herbertsmithite, the recent neutron scattering places an upper bound of 0.25 meV on any gap in the continuum of scattering. On the contrary, the continuum in $Rb_2Cu_3SnF_{12}$ is observed well above the sharp dispersive modes of the pinwheel VBS state. Thus, while pinwheel dimerization and DM interactions in $Rb_2Cu_3SnF_{12}$ induce resonant modes at low energies, it appears that a threshold in energy exists beyond which a spin flip is no longer a stable quasi-particle and the underlying quantum kagome nature of the material is apparent. Whether this scattering is best interpreted as resulting from two-magnon processes or magnon fractionalization will require a more detailed comparison between theories incorporating such features and higher quality scattering data.

$Cs_2Cu_3SnF_{12}$

Experiment and results

$Cs_2Cu_3SnF_{12}$ crystals were synthesized in accordance with the chemical reaction $2CsF + 3CuF_2 + SnF_4 \rightarrow Cs_2Cu_3SnF_{12}$. CsF, CuF_2 and, SnF_4 were dehydrated by heating in vacuum at about 100 ^oC. First the materials were packed into a Pt tube of 9.6 mm inner diameter and 100 mm length in the ratio of 3:3:2. One end of the Pt tube was welded and the other end was tightly folded with pliers and placed between Nichrome plates. Single crystals were grown from the melt. The temperature of the furnace was lowered from 850 to 750 ^oC over 100 hours. After collecting the well-formed pieces of crystal, we repeated the same procedure. Inelastic neutron scattering measurements were performed on two co-aligned single crystals of $Cs_2Cu_3SnF_{12}$ (total mass of 3.3 g) with a sample mosaic of about 1^o at GPTAS and HER, which are triple-axis spectrometers run by the Institute for Solid State Physics, University of Tokyo. At GPTAS, the final energy of the thermal neutrons was fixed at 14.7 meV. The collimations were 40'-40'-sample-40'-80'. A pyrolytic

graphite (PG) filter was placed after the sample to remove contamination from higher-order neutrons. The vertically focused (horizontally flat) PG crystals were used to analyze the scattered neutrons. At HER, the final energy of the cold neutrons was fixed at 5 meV. The scattered neutrons were analyzed using the central three blades of a seven-blade doubly focused PG analyzer. A cool Be or oriented-PG-crystal filter was placed in the incident beam and a room-temperature Be filter was placed in the scattered beam. In the analysis of the HER data, effective collimations of $10'-40'-sample-160'-120' were used. For both experiments, the sample was aligned with the (h, k, 0) plane horizontal to measure spin-wave excitations within the kagome plane. The sample was cooled to the base temperature of 3 K using a ^{4}He closed cycle cryostat.

Using the 2a x 2a enlarged unit cell for the low-temperature crystal structure, we observed an increased scattering intensity due to magnetic Bragg reflections below T_N=20.0 K at $\mathbf{Q}_m$=(2m, 2n, 0), where m and n are integers. The ordering wave vectors correspond to the reciprocal lattice points of the uniform kagome lattice above T_s=185 K. This result indicates that the ordered state has a **q**=0 structure. Hence the center of the 2D Brillouin zone located at Q_m is expected to give rise to strong spin-wave scattering.

Figure 4(a) shows constant-**Q** scans measured using the GPTAS spectrometer. The scans were performed at 3 K and at three different momentum transfers **Q**=(2, 2, 0), (2.25, 2, 0), and (2.267, 1.867, 0). At the zone center (Γ-point) **Q**=(2, 2, 0), we clearly observed two spin-wave excitations at 10.7(5) meV and 13.6(4) meV, and extra scattering above the background below 5 meV (top panel of Fig. 4(a)). A high-resolution measurement using the cold-neutron spectrometer HER revealed a spin gap of 1.0(6) meV as shown in Fig. 4(c). Away from the zone center along the $\Gamma \rightarrow \mathrm{M}$ and $\Gamma \rightarrow \mathrm{K}$ directions, we clearly observed three peaks representing three branches of spin-wave excitations, as shown in the middle and bottom panels of Fig. 4(a), respectively. Figure 4(b) shows constant-energy scans taken along two independent high-symmetry directions from the Γ-point to the M- and K-points. For both constant-**Q** and constant-energy scans, the peak width is resolution-limited and the line shape is well described by the convolution with the resolution function. As the temperature increases toward T_N, the energy of the spin gap Δ, which scales with

the order parameter, decreases toward zero and the peak width Γ, which is resolution-limited below 7 K, becomes broader, indicative of the shorter lifetime of the excitations, as shown in the inset of Fig. 4(c). Figures 5(a) and 5(b) show the spin-wave dispersions obtained from several constant-energy and constant-**Q** scans throughout the Brillouin zone along the two high-symmetry directions. The data points were obtained from resolution-convolution fits. Unfortunately, we were not able to determine the excitation energies of the high-energy modes owing to the high phonon background and low scattering intensity, which may be due to magnon instability.

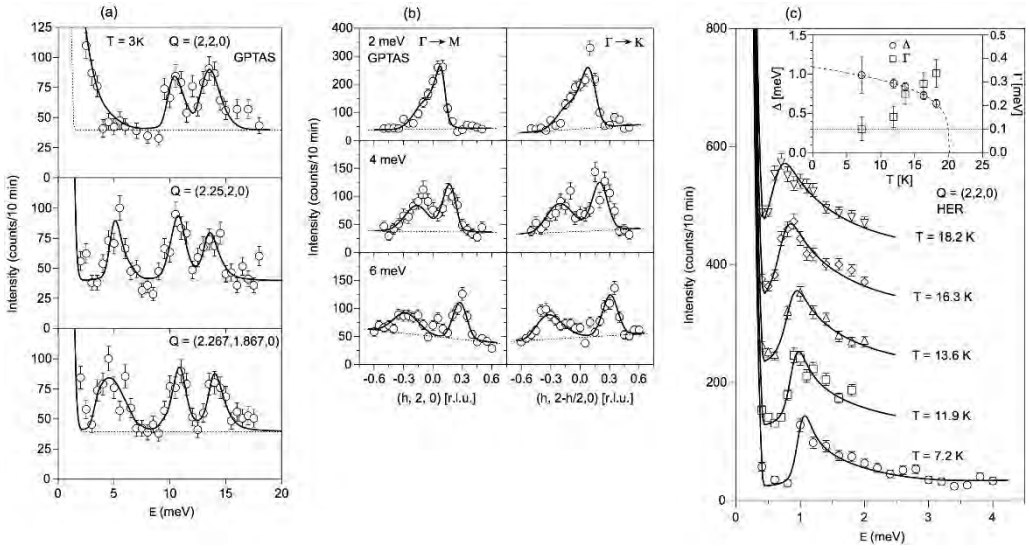

Figure 4. (a) Constant-**Q** scans measured at **Q**=(2, 2, 0), (2.25, 2, 0), and (2.267, 1.867, 0). (b) Constant-energy scans measured at $\hbar\omega$=2, 4, and 6 meV along two independent high-symmetry directions. (c) Temperature dependence of the spin gap at the Γ-point. The main panel shows constant-**Q** scans measured at the Γ-point at different temperatures. Data sets for different temperature are shifted vertically by 100. The inset shows the temperature dependences of the spin-gap energy Δ and peak width Γ. The dotted line denotes the resolution of the instrument obtained by the convolution fitting, and the dashed lines serve as a visual guide. The error bar denotes the statistical error.

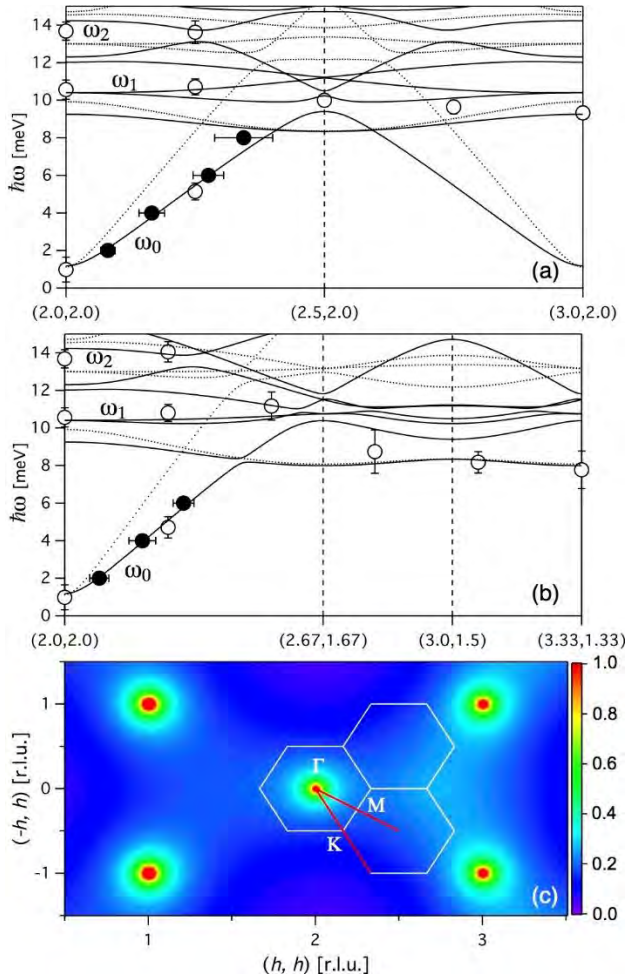

Figure 5. (a) and (b) Experimental data and calculated spin-wave dispersions along the two high-symmetry directions denoted by thick red lines in (c). Open symbols indicate the data measured around (2, 2, 0) while closed symbols indicate the data measured at the equivalent point around (0, 2, 0). Solid lines denote the best fit obtained using the DM model, and dotted lines denote dispersions with J_{avg}^{mag}=19.8 meV obtained from the magnetic susceptibility,J_2=-1.07 meV, d_z=-0.18, and d_p=0.033. (c) Calculated energy-integrated scattering intensity of $Cs_2Cu_2SnF_{12}$.

Discussion

We analyze the low-energy spin-wave dispersion observed in $Cs_2Cu_3SnF_{12}$ in the framework of LSWT. The underlying spin structure used to calculate the spin-wave dispersion is that of the **q**=0 structure for the uniform kagome lattice, in which all spins are oriented either

toward or away from the center of a triangle. In our previous study on $Rb_2Cu_3SnF_{12}$, we found that the DM interactions play a dominant role in singlet-triplet excitations, *i.e.*, a large out-of-plane component of the DM vectors gives rise to large splitting between the $S^z=\pm1$ and 0 modes and reduces the energy gap at the Γ-point. Therefore, as a first approximation, we consider the DM interactions as the dominant anisotropy energy (referred to as the DM model), and express the spin Hamiltonian as

$$H = \sum_{<ij>} \{J_{ij}(S_i \cdot S_j) + D_{ij} \cdot [S_i \times S_j]\} + J_2 \sum_{\ll k,l \gg} S_k \cdot S_l, \qquad (1)$$

where J_{ij} and J_2 are the nearest-neighbor (NN) and next-nearest-neighbor (NNN) exchange interactions, respectively, and D_{ij} are DM vectors. J_{ij} are nonuniform, and their magnitude is scaled by J_1, which can be written as $J_{1i}=a_iJ_1$ where i=1, 2, 3, and 4, while the strength of the DM vectors D_{ij} is scaled by the corresponding exchange interactions, $D^{\parallel}_{ij}=d_zJ_{ij}$ and $D^{\perp}_{ij}=d_pJ_{ij}$, where the configurations of the out-of-plane (in-plane) components of the DM vectors is $D^{\parallel}_{ij}$ ($D^{\perp}_{ij}$). We neglect the interlayer interaction, because the triplet excitations in $Rb_2Cu_3SnF_{12}$ are dispersionless perpendicular to the kagome layer.

The LSWT calculations of the spin-wave dispersion as well as the scattering intensity for the DM model of eq. 1, which are shown in Fig. 5, were performed using a symbolic algebra method written in Mathematica. The results reveal 12 branches of spin-wave excitations, but only three dominant low-energy branches are observed experimentally. The strong inelastic scattering intensity centered around $\mathbf{Q_m}$ (Fig. 5(c)) is consistent with the experimental data. The obtained fit parameters are J_1=13.6(3) meV, a_1=1 (fixed), a_2=1.0(1), a_3=0.84(7), a_4=0.70(5), J_2=-1.07(2) meV, d_z=-0.29(1) and d_p=0.057(4), giving $J^{sw}_{avg}=J_{11}+J_{12}+J_{13}+J_{14})/4$=12.1(7) meV. The solid lines in Figs. 5(a) and 5(b) represent the best fits with these parameters. The splitting of the two higher energy modes (ω_1 and ω_2, see Figs. 5(a) and 5(b)) at the Γ-point results from zone folding due to the structural transition. In the DM model, the energies of the ω_1 and ω_2 modes at the Γ-point are mainly determined by the out-of-plane component $D^{\parallel}$ of the DM vectors and the exchange

interactions. The value of $D^{\parallel}$ is as large as $0.29J_{1i}$, which is the same order of magnitude as the value of $D^{\parallel}$ observed in $Rb_2Cu_3SnF_{12}$. This large out-of-plane component of the DM vectors stabilizes the **q**=0 state, and thus is responsible for the magnetic ordering in $Cs_2Cu_3SnF_{12}$. For a uniform kagome lattice, the in-plane component $D^{\perp}$ gives rise to the splitting of the ω_1 and ω_2 modes and the spin gap Δ, which are expressed as ω_2-ω_1=2 $D^{\perp}$ $D^{\parallel}$ /(J_1+J_2) and $\Delta=\sqrt{3}\ D^{\perp}$, respectively. The large splitting of the ω_1 and ω_2 modes and the small spin gap Δ cannot be consistently described by the DM model with uniform J_1, attesting to the necessity of a spin model with the enlarged unit cell and nonuniform J_{1i}. The ω_1 branch, which corresponds to the zero-energy mode in the absence of the DM interactions, is lifted considerably owing to the large $D^{\parallel}$. Its weak dispersion and lowest spin gap at the K-point can be ascribed to a small ferromagnetic next-nearest-neighbor interaction (J_2<0). Another possibility accounting for the dispersion of the ω_1 mode is the quantum fluctuations, which are dominant for the spin-1/2 case and favor the $\sqrt{3}$ x $\sqrt{3}$ ordering at the K-point over the **q**=0 ordering.

Although the spin-wave dispersion observed in $Cs_2Cu_3SnF_{12}$ is qualitatively understandable in terms of LSWT and the DM model, there is a large quantitative disagreement between the exchange constant J_{avg} obtained from the spin-wave dispersion (J_{avg}^{sw}=12.1$ meV) and that obtained from the magnetic susceptibility data J_{avg}^{mag}=19.8$ meV. Here, we neglected the small in-plane component of the DM vector d_p. J_{avg}^{mag}=19.8 meV should be close to the true exchange constant. However, the dotted lines in Fig. 5(a) and (b), which represent LSWT with J_{avg}^{mag}, show a large discrepancy between the LSWT result and the data especially for the ω_0 mode. We note that the slope of this mode is predominantly determined by J_{avg}. Therefore, we deduce that the quantum fluctuations decrease excitation energies from those obtained by LSWT, *i.e.*, negative quantum renormalization of the excitation energies occurs in $Cs_2Cu_3SnF_{12}$. For a spin-1/2 triangular-lattice Heisenberg antiferromagnet, a recent theory predicts that at high energies spin-waves are strongly renormalized, so that the dispersion becomes flat. However, in contrast to the case of the triangular lattice, the renormalization factor ($R=J_{avg}^{sw}/J_{avg}^{mag}$=0.61) in $Cs_2Cu_3SnF_{12}$ appears to be independent of the momentum transfer.

We note the renormalization factors in other low-dimensional antiferromagnets. For $Cu(DCOO)_2 \cdot 4H_2O$, which is described as an S=1/2 square-lattice antiferromagnet, the positive quantum renormalization with R=1.21 was reported. This renormalization factor coincides with theoretical result. For Cs_2CuCl4, in which antiferromagnetic chains are coupled to form a spatially anisotropic triangular-lattice antiferromagnet, a large renormalization factor of R=1.63 was reported. This large positive quantum renormalization is attributed not to the triangular geometry of the lattice but to the spinon excitations characteristic of antiferromagnetic chain. For $KFe_3\ (OH)_6\ (SO_4)_2$, which is described as an S=5/2 uniform KLAF, the renormalization factor is estimated as R=0.90 using the exchange constants determined from the dispersion relations and magnetization and ESR measurements. This fact together with the present result on $Cs_2Cu_3SnF_{12}$ shows that the negative quantum renormalization of the excitation energies is universal for KLAFs with an ordered ground state and enhanced with decreasing spin quantum number S.

Unpublished Results

Study of magnetic excitations in $Cs_2Cu_3SnF_{12}$ using AMAERTAS

Magnetic excitations in the distorted kagome lattice antiferromagnet $Cs_2Cu_3SnF_{12}$ were measured using inelastic neutron scattering. The system is known to magnetically order at low temperatures below T_N = 20 K. The sample is aligned in (HHL) zone and cooled down to 7 K using a closed cycle He-4 cryostat. Two chopper configurations were used for two sets of accessible incident energies (E_i). In the first set-up, E_i of 27.64 meV, 11.67 meV, 6.403 meV, and 4.035 meV are accessible while in the second set-up, E_i of 51.04 meV, 16.98 meV, 8.388 meV and 4.988 meV are accessible. We found that E_i of 16.98 meV gives the optimal result in terms of the covering dynamic range and incident neutron flux.

Multiple datasets were acquired by rotating the sample about the vertical axis, which is parallel to [-1, 1, 0], in steps of 2˚ covering roughly 100˚ of sample orientation. The background was measured at 30 K, which is right above T_N, and 150 K for phonon background subtraction. These datasets were then combined to produce a background-subtracted, four-dimensional scattering-intensity function I(Q, $\hbar\omega$), where Q is momentum transfer and $\hbar\omega$ is energy transfer. However, in this report we will only show the data taken at 7 K. The data were sliced and cut along high symmetry directions using “Utsusemi” to produce contour maps. The scattering intensity is mapped along two diagonal directions namely [1,1] and [-1,1]. The latter is perpendicular to the scattering plane. The intensity is integrated along the [0,0,L] direction, taking advantage of non-dispersive and rod-like scattering along the L axis (Figure 6), which is a result of the two dimensionality of the system.

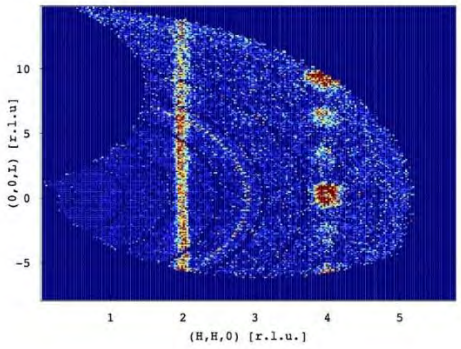

Figure 6. A intensity map shows the rod-like scattering along (0,0,L).

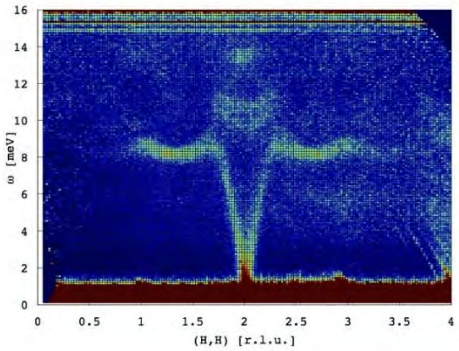

Figure 7. Spin-wave dispersion along (H,H)

The spin-wave dispersion along (H,H) shows a distinct feature (Figure 7). We observe the flat mode, which is a characteristic of the frustrated kagome lattice, indicative of highly degenerate connected states. In the high energy region, scattering intensity in the majority of the Brillouin zone vanishes, which can be a result of magnetic structure factor or more interestingly caused by magnon instability. We note that the magnetic excitations observed in this system is dramatically different from those observed in a closely related compound $Rb_2Cu_3SnF_{12}$, in which the magnetic

excitations are of a singlet-to-triplet type and scattering intensity is centered around the zone center.

The spin wave dispersion along (-H,H) shows the dispersive mode similar to that along (H,H) but the intensity of the flat mode becomes very weak along this direction as shown in Figure 6.

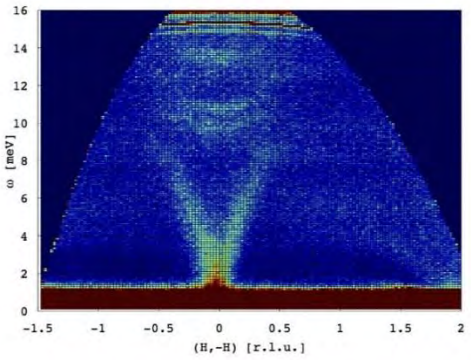

Figure 8. Spin-wave dispersion along (-H,H).

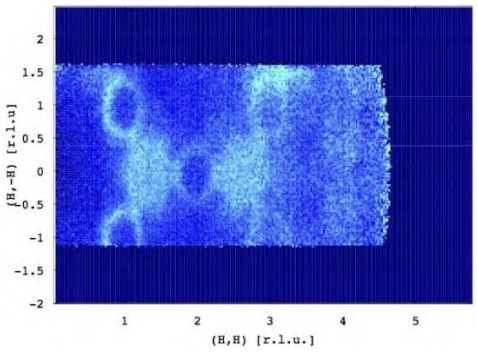

Figure 9. A intensity map in the (H,K) plane with an energy range [7.5-9] meV.

We note that the range of momentum transfer along (-H,H) is limited due to the smaller covering area of detector perpendicular to the scattering plane. The asymmetry of scattering intensity of the flat mode along (H,H) and (-H,H) can be best observed in the intensity map plotted in the (H,K) plane at an energy transfer range of 7.5 meV to 9 meV as shown in Figure 9. Our preliminary calculations of spin-wave intensity on this system show that this scattering intensity pattern can be reproduced assuming the q = 0 spin structure, where spins on each triangle points either toward or away from the center of the triangle, and non-uniform exchange interactions.

To summarize, we measured the spin-wave excitations in the distorted kagome lattice antiferromaget $Cs_2Cu_3SnF_{12}$ and observed the flat mode over extended region of the Brillouin zone. In addition, we observed the absence of scattering intensity in the high energy region, which could

be due to the structure factor or magnon instability. We are currently working on the analysis of these results. The preliminary analysis shows good agreement with the spin-wave calculations for low energy. However, the spin-wave result fails to explain the weak and broad scattering at high energy. Quantum renormalization and two magnon process could play a role in suppression or broadening of the magnetic excitations at high energy. Further work is required to understand these phenomena in the highly frustrated magnet.

Nuclear and magnetic structure study of $Cs_2Cu_3SnF_{12}$ using S-HRPD

Time-of-flight powder neutron diffraction was performed on the distorted kagome lattice antiferromagnet $Cs_2Cu_3SnF_{12}$ to study its nuclear and magnetic structure at low temperatures. A powder sample is filled in a 1cm-diameter vanadium can and cooled to base temperature of 10 K using a closed cycle He-4 cryostat. The data are collected by three detector banks, which we will called LA (low-angle bank), QA (90-degree bank), and BS (back-scattering bank) with the highest resolution. The measurements were done at four temperatures, 10 K (below T_N = 20 K), 25 K, which is right above T_N, 150 K (below T_f = 185 K, where the structural phase transition occurs), and 200 K. The counting time at each temperature is about 30 hours. After the data reduction process and normalization, the reduced scattering intensity of each detector bank is plotted as a function of either time-of-flight or d-spacing.

At the base temperature of 10 K. we observed magnetic Bragg peaks on top of the fundamental nuclear Bragg peaks at **Q** = (2,0,2) and (2,2,0). We note that the peaks are indexed using an approximate structure, where the space group is R-3, and the lattice parameters are *a* = 14.21 and *c* = 20.18, since the true structure at low temperature of this material is not yet known. Figure 10 shows extra scattering intensity at 10 K compared to the data the 25 K at (2,0,2) and (2,2,0) for the LA, QA and BS detectors, indicative of the magnetic Bragg peaks.

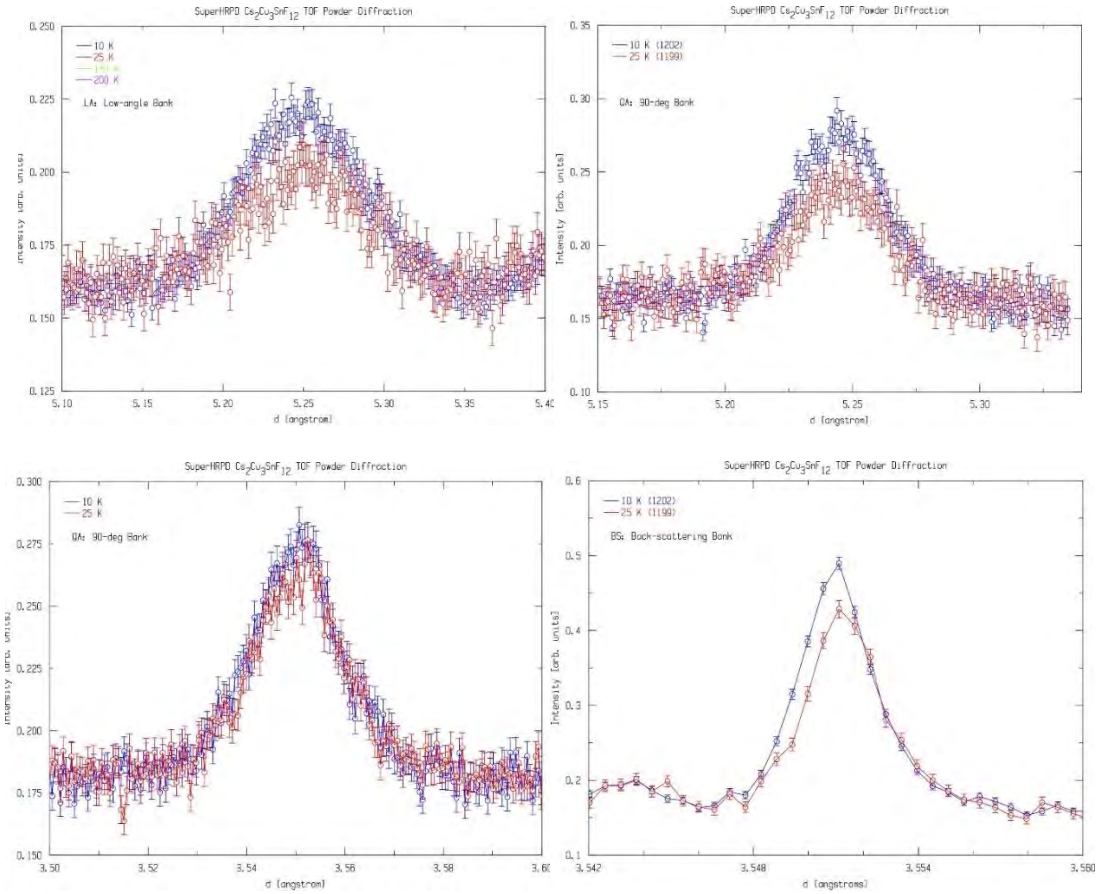

Figure 10. Top panels show the magnetic Bragg peak at (2,0,2) in the LA (left) and QA (right) detectors. Bottom panels show the magnetic Bragg peak at (2,2,0) in the QA (left) and BS (right) detectors.

At the structural phase transition, we observed the doubling of a unit cell, resulting in superlattice reflections. Figure 11 shows a group of superlattice peaks observed at 150 K but not at 200 K indexed by odd integers in H or/and K. These superlattice peaks are relatively small compared to the fundamental reflections; in the figure the fundamental reflections are (2,4,4) shown on the left and (0,0,9) shown on the right of the figure. In addition, we observed the splitting of the (2,4,4) peak suggesting that the true crystal structure is not exactly R-3. However, currently, the correct space group is unknown and further analysis is needed. We note that the splitting of some of the fundamental reflections can only observed using the high-resolution BS detector. The resolution of

the LA and QA detectors is not enough to resolve the splitting and hence the data from those two sets of detectors can be refined using the spaces group R-3.

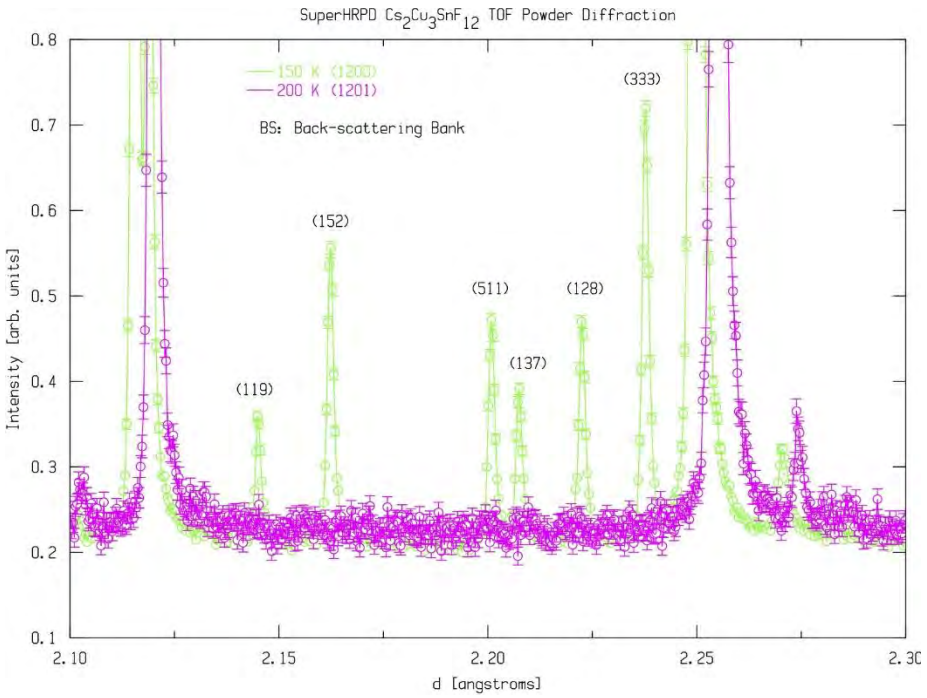

Figure 11. Superlattice reflections at odd integers in H or K between two fundamental reflections (2,4,4) at *d* = 2.112 angstroms, which splits into two peaks, and (0,0,9) at *d* = 2.112 angstroms, which does not split.

In summary, we performed high-resolution time-of-flight powder neutron diffraction on $Cs_2Cu_3SnF_{12}$ to study its nuclear and magnetic structure at low temperatures. We observed the magnetic Bragg peaks at 10 K, which disappears above T_N = 20 K. This magnetic peaks are very weak and lie on top of the structural peaks, making it difficult to detect. As the result, we can only observe two such magnetic peaks. In addition, we observed the superlattice peaks, which are due to the structural transition at T_f = 185 K. These superlattice peaks are small compared to the fundamental peaks indicative of small lattice distortion. Furthermore, the splitting of some fundamental Bragg peaks with even H and K is observed. The splitting is not observed at (0,0,L). This splitting of the fundamental peaks suggests that the symmetry of the crystal is not exactly R-3

as we have expected. We note that $Rb_2Cu_3SnF_{12}$, which is a closely related compound to $Cs_2Cu_3SnF_{12}$, crystallizes in R-3 at room temperature. This difference of the crystal structure could explain the observed difference in the magnetic ground states of these two compounds; while the ground state of $Rb_2Cu_3SnF_{12}$ is valence bond solid, S = ½ spins in $Cs_2Cu_3SnF_{12}$ magnetically order.

Study of magnetic excitations in doped $(Rb_{0.8}Cs_{0.2})_2Cu_3SnF_{12}$

The discovery of the pinwheel valence-bond-solid (VBS) state in the distorted kagome lattice antiferromagnet $Rb_2Cu_3SnF_{12}$ marks the first evidence of the VBS state in the approximate kagome lattice. In our previous work, we have measured the S=1 singlet-to-triplet excitations of the pinwheel VBS state using inelastic neutron scattering. Figure 12(a) shows the intensity map of the "flower-vase" shape of the triple excitations measured at the Cold Neutron Chopper Spectrometer (CNCS), the Spallation Neutron Source, Oak Ridge National Laboratory, USA. The system shows the quantum spin state, which has been proposed to be very close in energy to the ground state of the ideal kagome lattice. On the other hand, $Cs_2Cu_3SnF_{12}$, a close cousin of $Rb_2Cu_3SnF_{12}$, shows a magnetic-ordered Néel state. We have measured the spin-wave excitations of this distorted kagome antiferromagnet at AMATERAS, J-PARC, Japan. Figure 12(b) shows the intensity map of the "clione-like" (sea angle) shape of the spin-wave excitations, which has been discussed in the previous section.

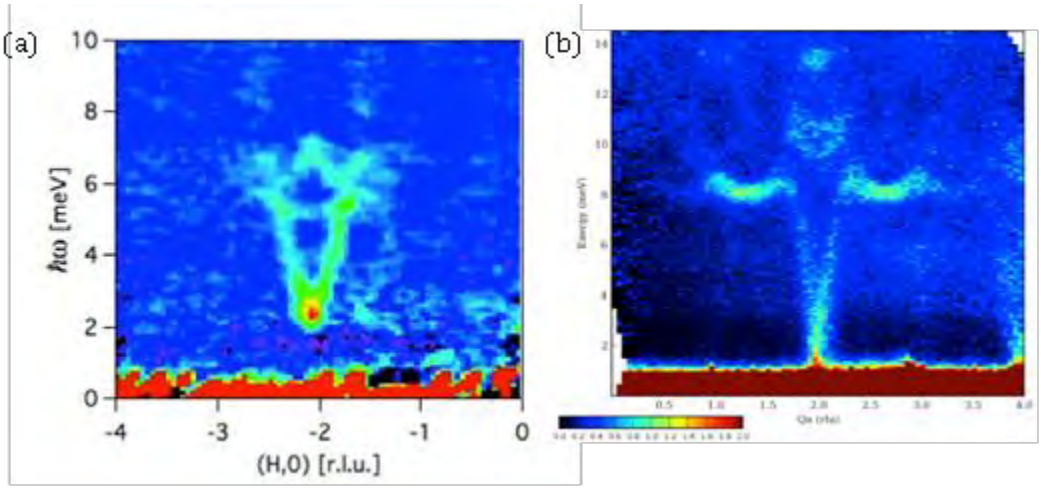

Figure 12. (a) Singlet-to-triplet excitations in a shape of “flower vase” were measured on single crystal $Rb_2Cu_3SnF_{12}$ at CNCS. (a) Spin-wave excitations in a “clione-like” shape were measured on single crystal $Cs_2Cu_3SnF_{12}$ at AMATERAS.

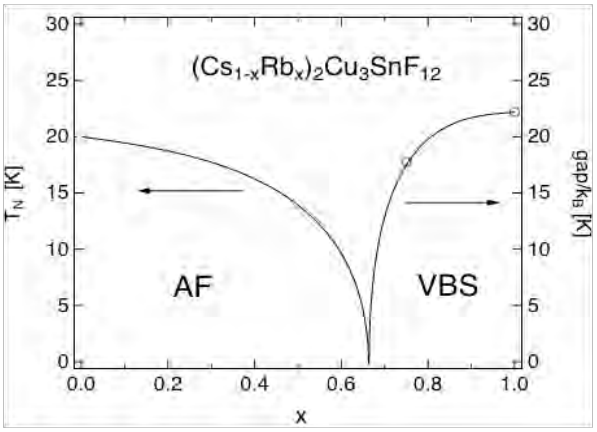

Figure 13. A phase diagram of $(Rb_xCs_{1-x})_2Cu_3SnF_{12}$ show the quantum phase transition at x ~0.3.

In doped $(Rb_xCs_{1-x})_2Cu_3SnF_{12,}$ preliminary thermodynamic-property measurements show that the system undergoes the quantum phase transition from the classical Néel state, which is characterized by T_N, to the VBS quantum state, which is identified by the presence of the single-to-triplet gap, at x ~ 0.7 as show in Figure 13. However, the precise nature of spin dynamics of the doped compound remains unclear. We, therefore, propose an experiment to resolve this issue by studying magnetic excitations in a doped compound $(Rb_xCs_{1-x})_2Cu_3SnF_{12}$ using inelastic neutron scattering. $(Rb_xCs_{1-x})_2Cu_3SnF_{12}$ crystallizes in the hexagonal R -3 space group with the estimate lattice constants, a = 14 .0(2) Å and c = 20.3(1) Å, depending on the value of x.

In this experiment, magnetic excitations in $(Rb_{0.8}Cs_{0.2})_2Cu_3SnF_{12}$ were studied using the neutron time-of-flight spectrometer AMASTERAS at J-PARC, Japan. A single crystal sample of mass ~3g was aligned in (HHL) zone and loaded into a closed cycle He-4 cryostat for cooling to a base temperature of 6 K. The chopper configuration is set up so that the energy of incident neutrons is 17 meV, which is the same configuration as that used in the similar measurements on $Cs_2Cu_3SnF_{12}$. The dataset was taken at several sample rotation covering about 100 degrees in a

step of 2 degree rotation. Background was measured at 50 K. The intensity is integrated along the [0,0,L] direction, taking advantage of non-dispersive and rod-like scattering along the L axis.

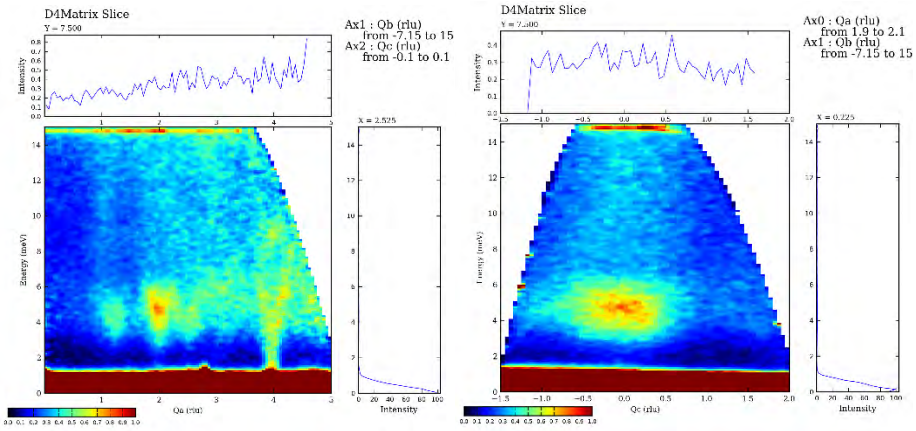

Figure 14. Scattering maps show magnetic excitations as a function of energy transfer and momentum transfer along [H,H] and [-H.H] directions

Figure 14 shows the scattering intensity maps measured at the base temperature of 6 K. Red denotes high intensity while dark blue denotes low intensity. The left panel shows magnetic excitations at (2,2,L) along (H,H) while the right panel shows the excitations along (-H,H). The measured scattering pattern is quite different from the magnetic excitations observed in both $Cs_2Cu_3SnF_{12}$ and $Rb_2Cu_3SnF_{12}$. The magnetic excitations appears to concentrate around the zone center and has a characteristic of a resonance scattering, that is, most of the scattering intensity concentrate within a small range of energy, in this case between 1-6 meV. Above 6 meV, the scattering become diffusive and relatively weak.

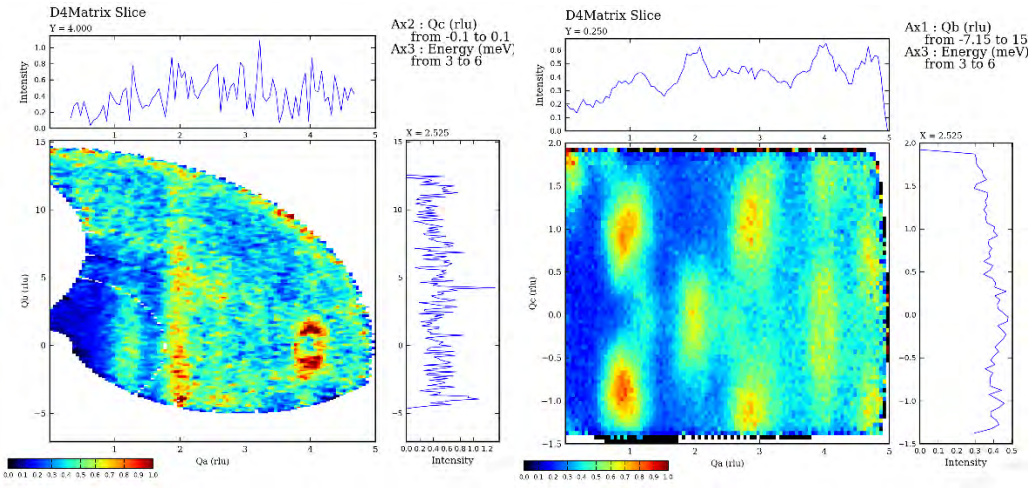

Figure 15. Scattering maps show magnetic excitations between energy transfer 3-6 meV as a function of momentum transfers [H,H,0] vs. [0,0,L] on the left panel and [H,H] vs. [-H,H] on the right panel. The energy is integrated from 3 meV to 6 meV.

Figure 15 shows energy-integrated scattering maps as a function of momentum transfers. The left panel shows the scattering rod along the L direction, attesting the two dimensionality of this system. The right panel show strong scattering intensity around the Brillouin zone centered at (2,2,L), (2,0,L) and (0,2,L).

In summary, we observe magnetic excitations in $(Rb_{0.8}Cs_{0.2})_2Cu_3SnF_{12}$ that are quite different from both in $Cs_2Cu_3SnF_{12}$ and in $Rb_2Cu_3SnF_{12}$. The origin of this scattering is not clear. One possibility is that the resonance scattering is intrinsic to this system. A less-interesting alternative is that it is due to randomness of exchange interactions caused by disordered doping. Further analysis is needed to distinguish between these two possibilities and examine other effects.

Synthesis and Characterization of α-$Cu_2V_2O_7$ Single Crystals

Experiment

Starting material of $Cu_2V_2O_7$ was prepared from high purity CuO and V_2O_5. The chemicals were dehydrated and weighed with stoichiometric ratio then ground thoroughly with ethanol. The mixture was calcined at 500 ˚C for 24 hours prior to the crystal growth process. The obtained

powder was inserted into a quartz tube. The bottom end of the tube was shaped into a taper for seed selection while the top end was tightly closed with silica wool. The sample was melted in the air at 850 ˚C for 10 h to ensure the homogeneity and then moved down through a constant temperature gradient of about 10 ˚C/cm with a rate of 1 cm/day. The sample was finally cooled from 700 ˚C to room temperature at a rate of 5 ˚C/min. The crystals were extracted from the quartz tube by mechanical separation. Small pieces of the crushed crystals were collected and ground for powder x-ray diffraction measurement then analyzed with the Rietveld refinement using FullProf. To further investigate the crystallinity and magnetic properties, single crystal neutron diffractions were measured with zero magnetic field at the BT-7 Double Focusing Thermal Triple Axis Spectrometer at the NCNR, USA. Magnetic susceptibility were measured to the base temperature of 5 K with a superconducting quantum interference device (MPMS-XL, Quantum De- sign) at Tohoku University, Japan.

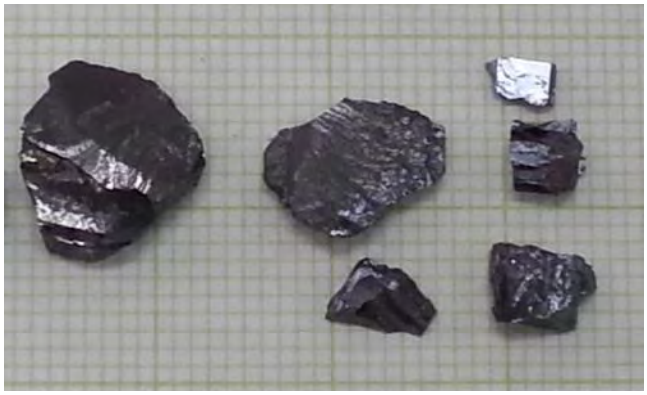

Figure 16. Single crystals α-Cu2V2O7.

Results and discussion

The obtained crystals are shown in Fig 16. The largest size of the crystals is about 1×1×0.5 cm^3 with a mass of more than 1 g. The cleaved facet is naturally (1,0,0) planes. Powder x-ray diffraction from the crushed with the Rietveld refinement gives lattice constants from the refinement a = 20.695(4) Å, b = 8.406(1) Å, and c = 6.450(1) Å, which is in good agreement with those reported in ref.12. The result shows that the major phase of the crystals is almost pure α-$Cu_2V_2O_7$ (about 98 wt %) with a small amount of impurities which can be indexed as β-Cu2V2O7 (the

(2,0,0) peak in Figure 17) and an unknown (* symbol), however we found from the elastic neutron scattering that this impurity and the β-Cu2V2O7 are showing up as the powder rings with a very low intensity. The impurities are however still presence after several tries with different cooling conditions which is an important parameter to control the phase as described by the previous studies. Our experiments found that the fraction of β-phase is getting higher compared to α-phase when the cooling rate is faster. Hence it is necessary to slowly cool the sample through the phase transition temperature at 712˚ to avoid the mixed phase.

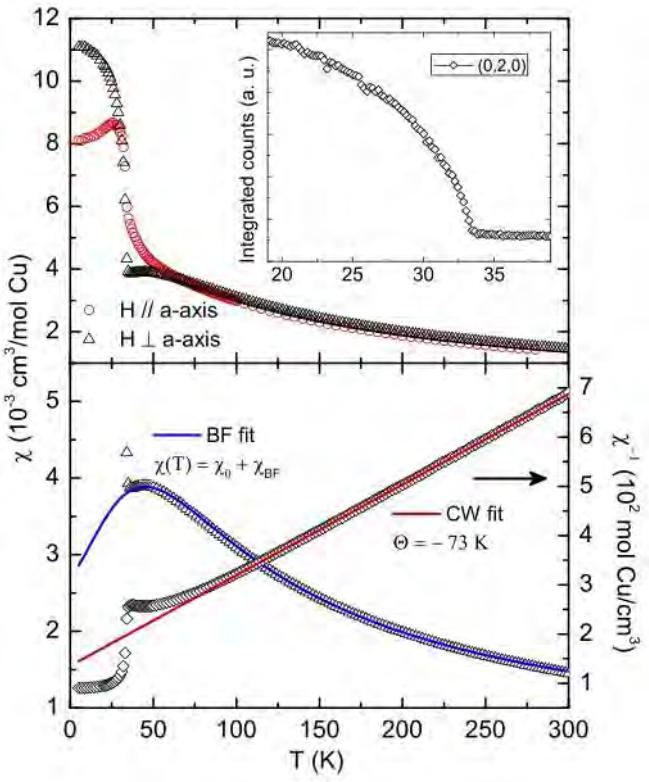

Figure 17. Magnetic susceptibility measurements. Upper panel shows the measurements from different crystallographic directions and the inset shows an order parameter measurement at (0,2,0) as a function of temperature. Lower panel shows both Bonner-Fisher fit and the Curie-Weiss law fit to the susceptibility with applied magnetic field parallel to the bc-plane.

Temperature dependence of magnetic susceptibility (χ = M/H) in the zero field-cooled mode (ZFC) is shown in Figure 17. The magnetic field is applied both parallel and perpendicular to the a-axis (upper panel). The susceptibility exhibits anisotropy and shows a sharp transition at

temperature 33 K consistent with the order parameter measurement from neutron scattering at (0,2,0) Bragg position (inset). The abrupt increase at 33 K is due to the transition from paramagnetic state to antiferromagnetic state with spins canting which is arising from Dzyaloshinskii-Moriya (DM) interaction and resulting in the weak magnetization. Above 100 K the fit of χ^{-1} vs T to the Curie-Weiss law (lower panel of Figure 17) gives a Curie constant of 0.54 cm^3/mol Cu and a negative Weiss temperature at -73 K. These values are in line with the previous results.

When the magnetic field is applied parallel to the a- axis a small cusp can be observed at the magnetic ordering transition. On the other hand, when the field is applied perpendicular to the a-axis (i.e. along the bc-plane) the susceptibility shows a broad maximum at around 50 K, which relates to 1D Heisenberg antiferromagnet, before an abrupt increase to the ordered state at lower temperature. The lower panel of Figure 17 shows the best fit to the Bonner-Fisher (BF) model for 1D S = 1/2 system

Reference

[1] A. P. Ramirez, in Handbook of Magnetic Materials (ed. Buschow, K.H.J.) Vol. 13, 423-520 (Elsevier Science, Amsterdam, 2001).

[2] C. Zeng and V. Elser, *Phys. Rev. B* **51**, 8318–8324 (1995).

[3] G. Misguich, D. Serban, and V. Pasquier, *Phys. Rev. Lett.* **89**, 137202 (2002).

[4] Y. Ran, M. Hermele, P. A. Lee, and X.-G. Wen, *Phys. Rev. Lett.* **98**, 117205 (2007).

[5] J. S. Helton, *et al.*, *Phys. Rev. Lett.* **98**, 107204 (2007).

[6] S.-H. Lee, *et al.*, *Nature Mater.* **6**, 853–857 (2007).

[7] F. Bert, *et al.*, *Phys. Rev. Lett.* **95**, 087203 (2005).

[8] M. Yoshida, M. Takigawa, H. Yoshida, Y. Okamoto, and Z. Hiroi, *Phys. Rev. Lett.* **103**, 077207 (2009).

[9] K. Matan, T. Ono, Y. Fukumoto, T. J. Sato, J. Yamaura, M. Yano, K. Morita, and H. Tanaka, accepted for publication in Nature Physics.

[10] B. Yang, and Y. B. Kim, *Phys. Rev. B* **79**, 224417 (2009).

[11] T.-H. Han, J. S. Helton, S. Chu, D. G. Nocera, J. A. Rodriguez-Rivera, C. Broholm, and Y. S. Lee, *Nature* **492**, 406 (2012)

[12] P. A. Lee, N. Nagaosa, and X.-G. Wen, *Rev. Mod. Phys.* **78**, 17 (2006), and references therein.

[13] Y. Taguchi, Y. Oohara, H. Yoshizawa, N. Nagaosa, and Y. Tokura, *Science* **291**, 2573–2576 (2001).

Published work in international journals

1. “Ghost modes and continuum scattering in the dimerized distorted kagome lattice antiferromagnet $Rb_2Cu_3SnF_{12}$,” **K. Matan**, Y. Nambu, Y. Zhao, T. J. Sato, Y. Fukumoto, T. Ono, H. Tanaka, C. Broholm, A. Podlesnyak, G. Ehlers, Physical Review B **89**, 024414 (2014).

2. “Large Negative Quantum Renormalization of Excitation Energies in the Spin-1/2 Kagome Lattice Antiferromagnet $Cs_2Cu_3SnF_{12}$,” T. Ono, **K. Matan**, Y. Nambu, T. J. Sato, K. Katayama, S. Hirata, H. Tanaka, Journal of Physical Society of Japan **83**, 043701 (2014).

Conference

“Negative quantum renormalization of excitation energies in the distorted kagome lattice antiferromagnet $Cs_2Cu_3SnF_{12}$,” K. Matan, American Physiccal Society March Meeting 2014, Denver Colorado.

Ghost modes and continuum scattering in the dimerized distorted kagome lattice antiferromagnet $Rb_2Cu_3SnF_{12}$

K. Matan,[1,2,*] Y. Nambu,[3] Y. Zhao,[4,5] T. J. Sato,[3] Y. Fukumoto,[6] T. Ono,[7] H. Tanaka,[8,†] C. Broholm,[5,9,10] A. Podlesnyak,[10] and G. Ehlers[10]

[1]*Department of Physics, Faculty of Science, Mahidol University, Bangkok 10400, Thailand*
[2]*ThEP, Commission of Higher Education, Bangkok 10400, Thailand*
[3]*IMRAM, Tohoku University, Sendai, Miyagi 980-8577, Japan*
[4]*Department of Materials Science and Engineering, University of Maryland, College Park, Maryland 20742, USA*
[5]*NIST Center for Neutron Research, National Institute of Standards and Technology, Gaithersburg, Maryland 20899, USA*
[6]*Department of Physics, Faculty of Science and Technology, Tokyo University of Science, Noda, Chiba 278-8510, Japan*
[7]*Department of Physical Science, School of Science, Osaka Prefecture University, Sakai, Osaka 599-8531, Japan*
[8]*Department of Physics, Tokyo Institute of Technology, Meguro-ku, Tokyo 152-8551, Japan*
[9]*Institute for Quantum Matter and Department of Physics and Astronomy, The Johns Hopkins University, Baltimore, Maryland 21218, USA*
[10]*Quantum Condensed Matter Division, Oak Ridge National Laboratory, Oak Ridge, Tennessee 37831, USA*

(Received 17 May 2013; revised manuscript received 27 December 2013; published 21 January 2014)

High-intensity pulsed neutron scattering reveals a new set of magnetic excitations in the pinwheel valence-bond solid state of the distorted kagome lattice antiferromagnet $Rb_2Cu_3SnF_{12}$. The polarization of the dominant dispersive modes (2 meV $< \hbar\omega <$ 7 meV) is determined and found consistent with a dimer series expansion with strong Dzyaloshinskii–Moriya interactions ($D/J = 0.18$). A weakly dispersive mode near 5 meV and shifted "ghosts" of the main modes are attributed to the enlarged unit cell below a $T = 215$ K structural transition. Continuum scattering between 8 and 10 meV might be interpreted as a remnant of the kagome spinon continuum [Nature (London) **492**, 406 (2012).].

DOI: 10.1103/PhysRevB.89.024414 PACS number(s): 75.10.Kt, 75.10.Jm, 78.70.Nx

I. INTRODUCTION

Interacting spins on the two-dimensional kagome lattice have fascinated physicists since Syozi first showed that Ising spins on this lattice, which he named after the woven pattern on a Japanese bamboo basket, do not order for $T \to 0$ [1]. More recently, efforts have focused on determining the ground state of the quantum spin-$\frac{1}{2}$ Heisenberg kagome lattice antiferromagnet, which is considered to be one of the most challenging problems in condensed matter physics. The complexity arises from the macroscopic degeneracy caused by the incompatibility between the global geometry of the corner-sharing triangular network and local, nearest-neighbor antiferromagnetic interactions [2]. The classical Néel state is apparently replaced by a dynamic quantum state, the details of which remain to be established. Proposed ground states include a gapless U(1)-Dirac-spin-liquid state [3–6], a gapped-spin-liquid [7–11], and valence-bond-solid (VBS) states [12–16]. These states are very close in energy so small perturbations and intrinsic limitations of numerical methods make it difficult to reach a firm conclusion. Most of the recent theoretical studies point to a quantum spin liquid [17] although there is no consensus on its precise nature.

Identifying an ideal kagome lattice model system has also proven to be difficult. All realizations so far have been plagued by magnetic impurities, lattice distortion, and extra terms in the spin Hamiltonian including anisotropic and further-neighbor interactions [18–28]. Albeit minuscule in some cases, these effects may conceal the intrinsic nature of the nearest-neighbor Heisenberg kagome antiferromagnet (HKAFM). Still, much can be learned by studying materials with interacting quantum spins on kagome-like lattices. For the quantum spin-$\frac{1}{2}$ kagome lattice antiferromagnet $ZnCu_3(OH)_6Cl_2$ (herbertsmithite), a recent experiment by Han *et al.* indicates that fractionalized excitations, a key characteristic of spin liquids, are robust against a small excess of Cu^{2+} ions in the interlayer sites and against anisotropic Dzyaloshinskii–Moriya (DM) interactions [29]. The recent discovery of the pinwheel VBS state in the distorted kagome lattice antiferromagnet $Rb_2Cu_3SnF_{12}$ offers a rare opportunity to study a cooperative singlet on an approximate kagome lattice [30]. Besides being unique and interesting in its own right, the pinwheel VBS state may display intersite correlations and excitations related to the ideal HKAFM [31].

At room temperature, $Rb_2Cu_3SnF_{12}$ has the hexagonal $R\bar{3}$ space group with lattice parameters $a = 13.917(2)$ Å and $c = 20.356(3)$ Å [32]. At 215 K, it undergoes a first-order structural transition, doubling the in-plane lattice constant a. The resulting lattice distortion is small [30] so to a first approximation we use the room-temperature structure, where a two-dimensional unit cell comprises 12 Cu^{2+} spins [Fig. 1(a)]. The spin-$\frac{1}{2}$ Cu^{2+} ions form a distorted kagome plane and are surrounded by a deformed octahedral environment of fluorine. The kagome planes are separated by nonmagnetic ions, which results in weak interlayer interactions. The distorted kagome lattice gives rise to four antiferromagnetic in-plane exchange interactions $J_1 > J_2 > J_3 > J_4$ [Fig. 1(a)]. To lowest order, spins interacting through J_1 form singlets which are linked through the weaker interactions. Powder neutron diffraction shows no magnetic order down to 1.3 K. The low-temperature magnetic susceptibility indicates a nonmagnetic, spin singlet ($S_{\text{tot}} = 0$) ground state and mixing of the singlet and triplet

*kittiwit.mat@mahidol.ac.th
†tanaka@lee.phys.titech.ac.jp

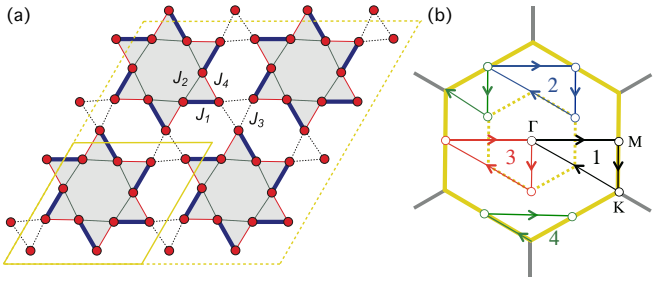

FIG. 1. (Color online) (a) The pinwheel VBS state is formed by dimers (thick lines). A dimer is a pair of spins with the largest exchange interaction J_1. The exchange interactions are $J_1 > J_2 > J_3 > J_4$. Yellow solid lines denote a two-dimensional unit cell of the room-temperature phase while yellow dotted lines denote the $2a \times 2a$ enlarged unit cell. (b) A diagram showing paths 1, 2, 3, and 4 in the first Brillouin zone. The dotted hexagon denotes the smaller Brillouin zone associated with the enlarged unit cell.

($S_{\text{tot}} = 1$) excited states through the DM interactions [33] (S_{tot} denotes the quantum number for the total spin of a single dimer). To a good approximation, the spin Hamiltonian is given by

$$\mathcal{H} = \sum_{nn} \left[J_{ij} \mathbf{S}_i \cdot \mathbf{S}_j + \mathbf{D}_{ij} \cdot \mathbf{S}_i \times \mathbf{S}_j \right], \qquad (1)$$

where $J_{ij} > 0$ are the nearest-neighbor antiferromagnetic exchange interactions, and $\mathbf{D}_{ij}$ are the corresponding DM vectors.

In a previous study [30] involving several of the present authors, magnetic excitations from the singlet ground state were probed using inelastic neutron scattering on a triple-axis spectrometer. These measurements revealed the pinwheel motif of dimers and determined the relevant spin Hamiltonian parameters through a dimer series expansion up to eighth order. However, the detailed structure of the excitations could not be resolved due to lack of resolution and counting statistics (see Fig. 2 in Ref. [30]). Here we report high-intensity pulsed neutron scattering measurements on single crystalline $Rb_2Cu_3SnF_{12}$ using the Cold Neutron Chopper Spectrometer at the Spallation Neutron Source, Oak Ridge National Laboratory [34]. A time-resolved, highly pixelated detector system that covers a large solid angle (14% of the unit sphere) enabled concurrent measurements over a much wider range of momentum and at higher resolution than previously. We confirm the splitting of the triplet associated with dimerization into a doublet and a singlet as a result of strongly anisotropic interactions and are able to unambiguously determine the polarization of each mode. More importantly, we discover a new family of modes associated with the structural superlattice, and a continuum at high energy, which may be related to the spinon continuum recently detected in the undimerized kagome system, herbertsmithite [29].

The article is organized as follows: In Sec. II, we describe the inelastic neutron scattering experiment and the resulting data. In Sec. III A, the measured magnetic excitations are analyzed in the framework of a dimer series expansion for the $2a \times 2a$ enlarged unit cell. We find very good agreement for energy transfer less than 8 meV. We analyze the wave-vector dependence of scattering perpendicular to the kagome planes to determine the magnetic polarization of each mode in Sec. III B. This confirms that the triplet is split into a singlet and a doublet. Section III C is devoted to a discussion of the excitation spectrum and continuum scattering between 8 and 10 meV, which cannot be explained by the dimer series expansion. We end with a summary in Sec. IV.

II. EXPERIMENT AND RESULTS

Single-crystalline $Rb_2Cu_3SnF_{12}$ was synthesized from the melt using the method described in Ref. [33]. Inelastic neutron scattering measurements were performed on two co-aligned crystals with a total mass of 4 g and a mosaic of 1.5°. The sample was mounted with the $(H,0,L)$ reciprocal lattice plane horizontal to allow intensity integration of rod-like scattering along the L direction while taking advantage of the two dimensionality of the system. The incident energy E_i was fixed at 12 meV for an energy resolution (full width at half maximum) of 0.56(3) meV at the elastic position. The sample was cooled to a base temperature of 2 K using a He-4 cryostat. Multiple datasets were acquired by rotating the sample about the vertical axis, which is parallel to $[-1,2,0]$, in steps of 2° covering 68° of sample orientation. An angle between the incident beam and $[0,0,1]$ ranges from −28.5° to 39.5°. The background was measured at 70 K, where the excitations are very broad and weak [30]. These datasets were subsequently combined to produce a background-subtracted, four-dimensional scattering-intensity function $I(\mathbf{Q},\hbar\omega)$, where $\mathbf{Q}$ is the momentum transfer and $\hbar\omega$ is the energy transfer. The data were sliced and cut along high-symmetry directions using MSLICE [35] to produce contour maps and constant-$\mathbf{Q}$ and constant-energy plots.

A contour map of $\hbar\omega \cdot I(\mathbf{Q},\hbar\omega)$ averaged over the L direction (the L dependence of the scattering intensity will be discussed later), which is plotted as a function of energy and in-plane momentum along $[H,0]$ [Fig. 2(a)], shows a distinct pattern of excitations around $(-2,0)$ and faint outlines of similar patterns displaced by $\Delta H = \pm 4$. The latter are barely detectable around the equivalent Brillouin-zone centers, $(-6,0)$ and $(2,0)$. The measurements were set up so integration along L is optimal at $(-2,0)$. The difference in the intensity profile around $(-2,0)$ and $(2,0)$ is a result of a smaller range of intensity integration for the latter. The overall profile of the excitations around $(-2,0)$ is consistent with our previous report [30]. The lower branch, which has a broader bandwidth, is known to be a twofold-degenerate excitation as it is split by a magnetic field along the c direction [30]. By mapping the L dependence of the intensity of this branch, we shall later show that it is associated with transitions from the singlet ground state ($S_{\text{tot}} = 0$) to a doublet with $S_{\text{tot}} = 1$ and $S_{\text{tot},z} = \pm 1$ ($S_{\text{tot},z}$ denotes the magnetic quantum number of the $S_{\text{tot}} = 1$ triplet states). The upper branch, which has a smaller bandwidth, does not split in a field and so is thought to be a nondegenerate excitation from the singlet ground state to the singlet state with $S_{\text{tot}} = 1$ and $S_{\text{tot},z} = 0$. We note that these states are not pure states of defined angular momentum due to the DM interactions.

A constant-$\mathbf{Q}$ cut at $(-2,0)$ [Fig. 2(d)] shows clear resolution-limited peaks at $\hbar\omega = 2.4(3)$ and 6.9(3) meV, consistent with the previous data (where the uncertainty represents half the energy resolution). The contour maps around the zone

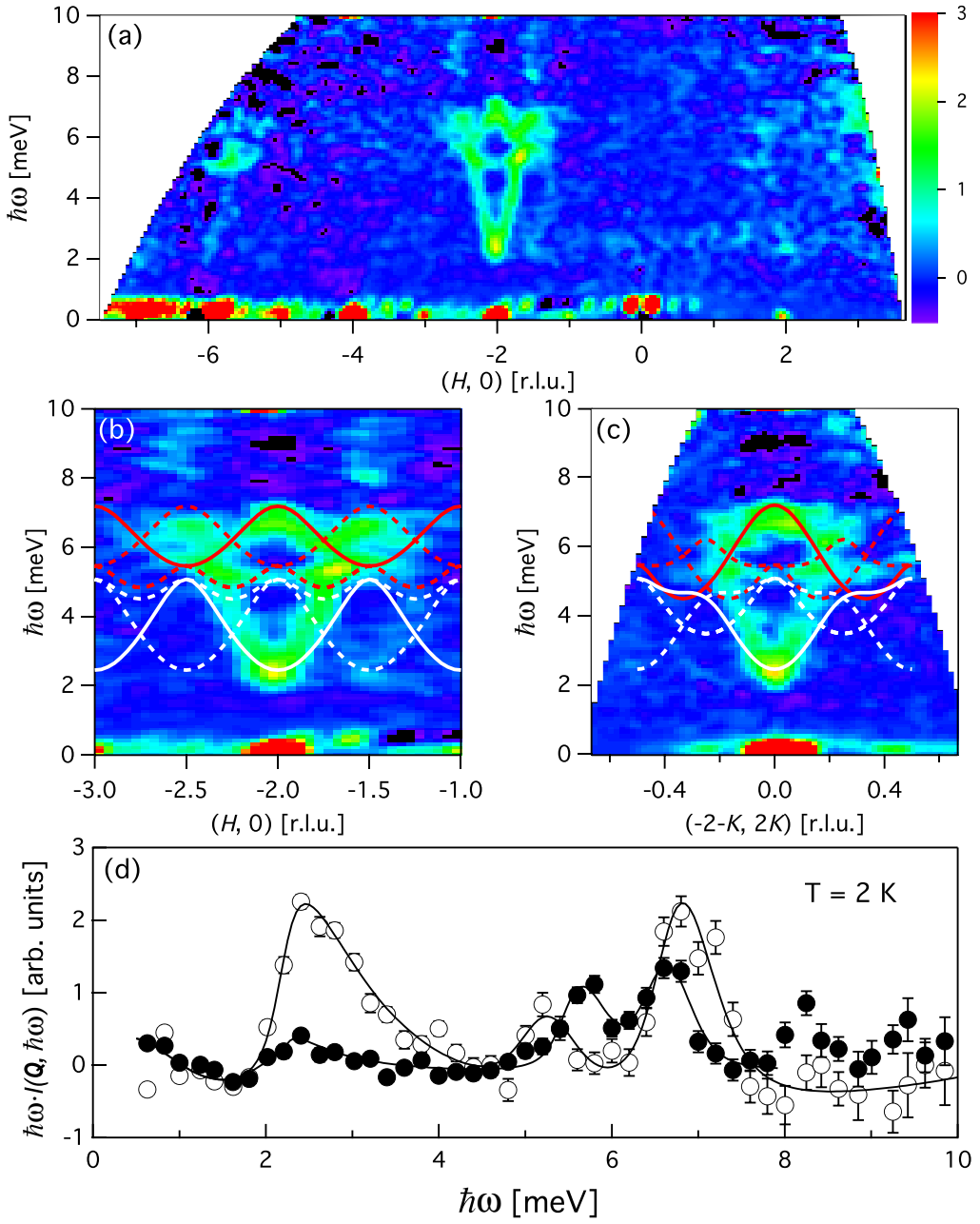

FIG. 2. (Color online) Contour maps show a product of scattering intensity and energy transfer $\hbar\omega \cdot I(\mathbf{Q},\hbar\omega)$, displaying magnetic excitations in $Rb_2Cu_3SnF_{12}$ as a function of energy and in-plane momentum through (a), (b) $(H,0)$ and (c) $(-2-K,2K)$. The intensity is averaged over the available range of L, $\Delta\mathbf{Q}_{[1,0]}$ of 0.042 Å^{-1}, and $\Delta\mathbf{Q}_{[-1,2]}$ of 0.045 Å^{-1}. The measurements along $[-K,2K]$ are limited by a smaller detector-coverage area perpendicular to the horizontal plane. Solid lines represent the excitations of the original spin Hamiltonian whereas dotted lines denote excitations resulting from the $2a \times 2a$ enlarged unit cell. Red denotes the $S_{\mathrm{tot},z} = 0$ mode and white denotes the $S_{\mathrm{tot},z} = \pm 1$ mode. (d) Constant-**Q** cuts show $\hbar\omega \cdot I(\mathbf{Q},\hbar\omega)$ at $(-2,0)$ (open circles) and the average of $\hbar\omega \cdot I(\mathbf{Q},\hbar\omega)$ at $(-1.5,0)$ and $(-2.5,0)$ (closed circles). Above 8 meV, the closed symbols lie above background, indicative of the continuum scattering. The lines are guides to the eye. The error bar represents one standard deviation.

center $(-2,0)$ [Figs. 2(b) and 2(c)] reveal a more intricate set of excitations than previously appreciated. A weakly dispersive mode around 5 meV is visible along both $[H,0]$ and $[-K,2K]$ [Figs. 2(b) and 2(c)]. At the zone center this mode peaks at 5.3(3) meV [Fig. 2(d)]. It grows slightly more intense away from the zone center, which contrasts with the other two modes that become weaker. We also observe excitations centered around $(-1.5,0)$ and $(-2.5,0)$ [Figs. 2(b) and 5(a) (2.0 to 2.5 meV)], which resemble the mode around $(-2,0)$, but with much less intensity, and hence are named the "ghost" modes. We have previously reported these ghost modes and attributed them to the enlarged unit cell caused by the structural transition [30]. Our dimer series expansion shown by solid lines in Figs. 2(b) and 2(c) and the bond-operator mean-field theory

[36] cannot account for all of this observed scattering intensity between 2 and 7 meV as neither calculation considers the enlarged unit cell. Furthermore, we observe diffuse scattering between 8 and 10 meV near $(-1.5,0)$ and $(-2.5,0)$, which cannot be accounted for by the dimer series expansion.

III. ANALYSIS AND DISCUSSION

In this section, we first analyze the excitation dispersions below 8 meV using the extended version of the dimer series expansion, which has been discussed in our previous work [30], to include the effect of the enlarged unit cell. We then investigate the L dependence of the intensity to determine the polarization of each mode. We end this section with a discussion of the diffuse scattering between 8 and 10 meV.

A. Dimer series expansion and enlarged unit cell

To understand the 5 meV mode and the ghost modes around $(-1.5,0)$ and $(-2.5,0)$, we consider the $2a \times 2a$ enlarged unit cell consisting of 48 spins shown in Fig. 1(a). We write the spin Hamiltonian as $\mathcal{H} + H'$, where $\mathcal{H}'$ represents a perturbation due to the enlarged unit cell. $\mathcal{H}'$ has the exact same form as $\mathcal{H}$ [Eq. (1)] but the sum is over 48 spins in the enlarged unit cell [see Fig. 1(a)]. We then perform the dimer series expansion on the pinwheel VBS state using the Hamiltonian $\mathcal{H} + H'$. The linked cluster expansion algorithm was used to generate a graphical series of dimers [37]. The low-energy spectra are calculated up to eighth order in the interdimer and DM interactions using the Dlog–Padé approximation [30]. We define the path $\Gamma \rightarrow M \rightarrow K \rightarrow \Gamma$ in the first Brillouin zone of the original model $\mathcal{H}$ as path 1 [Fig. 1(b)]. The lowest-energy excitations with $S_{\mathrm{tot},z} = \pm 1$ and those with $S_{\mathrm{tot},z} = 0$ along path 1 are shown in Fig. 3(a). We also define paths 2, 3, and 4 [Fig. 1(b)], which differ by a reciprocal lattice vector of the enlarged unit cell. Dispersion curves for paths 2, 3, and 4 are shown in Figs. 3(b), 3(c), and 3(d), respectively. In Figs. 2(b) and 2(c) path 1 shown as solid lines and paths 2, 3, and 4 shown as dotted lines are qualitatively in agreement with the data. If $\mathcal{H}'$ is nonzero but very small, then paths 2, 3, and 4 become equivalent to path 1, and the dispersion curves shown by dotted lines are the anticipated ghost modes together with the corresponding excitations of the original Hamiltonian.

It is interesting to note that the weakly dispersive mode in Fig. 2(b) is originally the excitation on the path between two adjacent M points [paths 2 and 4 in Fig. 1(b)]. From the experiment, this mode is not symmetric around $H = -1.75$; its energy increases monotonically as H varies from -2 to -1.5. This suggests that we observe the $S_{\mathrm{tot},z} = \pm 1$ triplet excitations around the zone center, $H = -2$, and the $S_{\mathrm{tot},z} = 0$ triplet excitations away from there, which may be experimentally verified by measurements in a magnetic field. We note that the in-plane component of the DM vector d_p is set to zero in our dimer series expansion. A recent ^{63,65}Cu NMR study in high fields up to 30 T [38] and neutron scattering measurements [39] show that the mixing between the singlet and triplet states via the DM interactions gives rise to a large residual gap. The anticrossing of the singlet and triplet mode, which is due to the combined effect of the off-diagonal g tensor and small d_p ($|d_p| < 0.012$) [38], prevents the gap from closing at high magnetic fields. However, d_p has little effect on the overall zero-field spectrum [30].

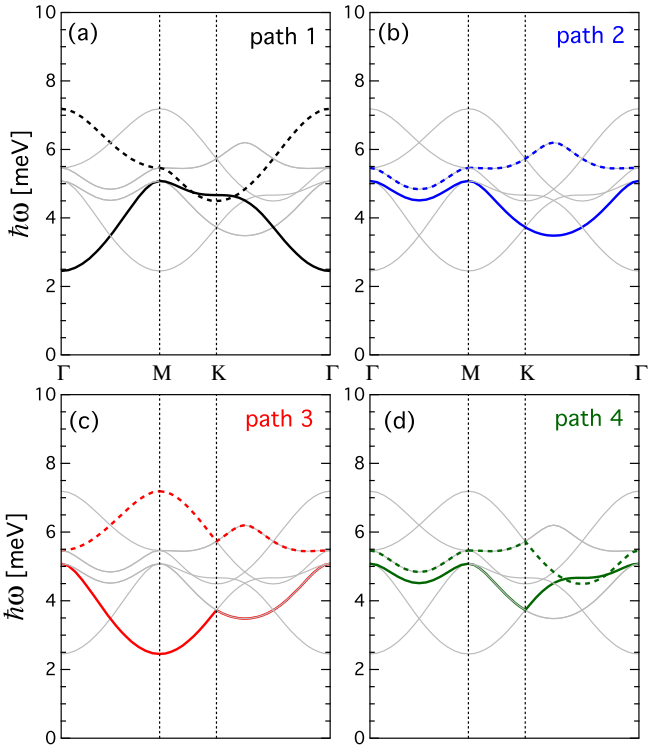

FIG. 3. (Color online) (a) Singlet-to-triplet excitations along path 1 [Fig. 1(b)] for the unperturbed Hamiltonian $\mathcal{H}$ are shown by black lines. Gray lines denote the modes resulting from the perturbed Hamiltonian $\mathcal{H}'$ associated with the enlarged unit cell. Solid lines denote excitations from the singlet ground state to the $S_{\mathrm{tot},z} = \pm 1$ states whereas dotted lines denote excitations to the the $S_{\mathrm{tot},z} = 0$ state. Colored solid and dotted lines in panels (b), (c), and (d) show the excitations along paths 2, 3, and 4 [Fig. 1(b)], respectively.

B. L dependence and mode polarization

The scattering intensity displayed thus far was averaged over the L direction. However, the L dependence of the scattering intensity contains valuable information about the polarization of the excitations and interplane correlations. Within the resolution of our measurements, there is no dispersion along L [Fig. 4(a)], which attests to the two-dimensional nature of the system. Contour maps of the scattering intensity integrated over the energy ranges $\hbar\omega = [2.0,3.0]$ meV [Fig. 4(b)] and $\hbar\omega = [6.5,7.5]$ meV [Fig. 4(c)] plotted as a function of H and L show rods of scattering that extend along L at $H = -6$, -2, and 2. The integrated intensity of the $S_{\mathrm{tot},z} = \pm 1$ mode has broad maxima at $L = 3$ and 6 before falling off at large L [Fig. 4(d)], while that of the $S_{\mathrm{tot},z} = 0$ mode monotonically decreases as a function of L with a small hump around $L = 6$ [Fig. 4(e)]. The overall trend of the curves reflects the different polarization of the modes while the modulation of scattering intensity results from interplane correlations. The magnetic scattering cross section

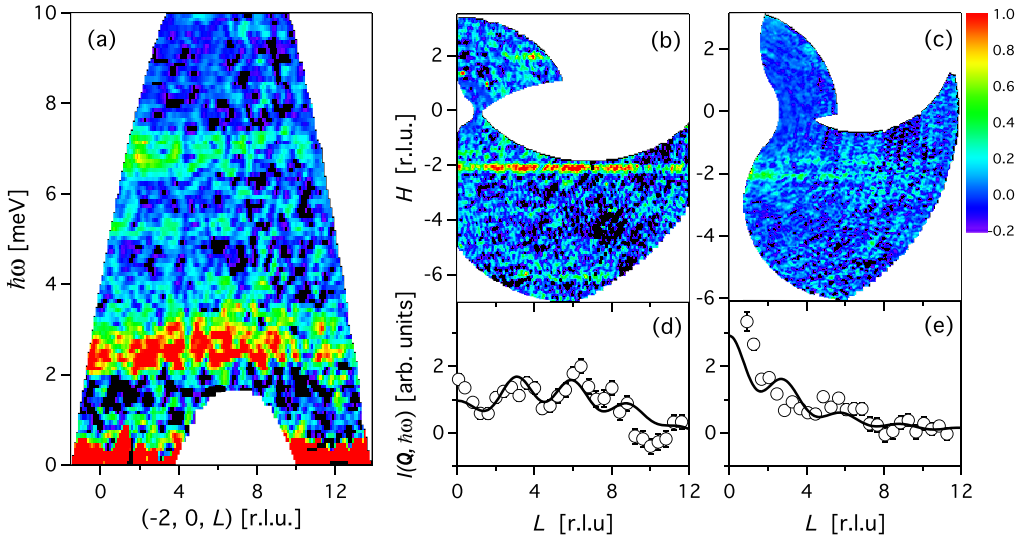

FIG. 4. (Color online) (a) Contour maps of $I(\mathbf{Q},\hbar\omega)$ are plotted as a function of $\hbar\omega$ and L. The intensity is averaged over $\Delta\mathbf{Q}_{[1,0]}$ of 0.042 Å^{-1} and $\Delta\mathbf{Q}_{[-1,2]}$ of 0.045 Å^{-1}. The broadening is a result of the integration along the in-plane momenta. Panels (b) and (c) show contour maps of $I(\mathbf{Q},\hbar\omega)$ plotted as a function of H and L. The intensity is energy integrated for (b) $\hbar\omega = [2.0,3.0]$ meV and (c) $\hbar\omega = [6.5,7.5]$ meV. Panels (d) and (e) show the L dependence of $I(\mathbf{Q},\hbar\omega)$ for energy ranges (d) $\hbar\omega = [1.0,4.0]$ meV and (e) $\hbar\omega = [6.0,8.0]$ meV centered at $(-2,0)$. The intensity is averaged over $\Delta\mathbf{Q}_{[1,0]}$ of 0.10 Å^{-1} and $\Delta\mathbf{Q}_{[-1,2]}$ of 0.18 Å^{-1}. Solid lines denote the product of the magnetic form factor for Cu^{2+} spins, the interplane correlation function, and the polarization factor, assuming that modes are polarized (d) in the kagome plane and (e) out of the plane.

[40] can be described by

$$\frac{d^2\sigma}{d\Omega dE'} = N_M \frac{\mathbf{k}'}{\mathbf{k}}(\gamma r_0)^2 \left[\frac{g}{2} f(\mathbf{Q}) e^{-W}\right]^2 \times \sum_{\alpha,\beta}(\delta_{\alpha\beta} - \hat{Q}_\alpha \hat{Q}_\beta) S^{\alpha\beta}(\mathbf{Q},\omega), \quad (2)$$

where the $\mathbf{Q}$-dependent terms are the magnetic form factor $f(\mathbf{Q})$ and the dynamic magnetic structure factor $S^{\alpha\beta}(\mathbf{Q},\omega)$, which is the space and time Fourier transform of the spin-pair correlation function. The magnetic scattering cross section also contains the polarization factor that arises from the anisotropy of the dipole-dipole interaction between neutrons and electrons.

For the magnetic excitations in $Rb_2Cu_3SnF_{12}$, the polarization factor becomes $1 \underset{(-)}{+} (Q_L/|\mathbf{Q}|)^2$, where Q_L is a component of $\mathbf{Q}$ along L. It grows (shrinks) with increasing L if the polarization is in plane or transverse (out of plane or longitudinal) [40]. The interplane correlations, which are embedded in the dynamic structure factor, can be described by a function $1 + \alpha\cos(\frac{2\pi L}{3})$, when the correlations along c only extend to the nearest-neighbor plane located at $\frac{c}{3}$. Here the fit parameter α indicates the type and strength of interplane correlations. (Ferromagnetic for positive α, antiferromagnetic for negative α.) The product of the magnetic form factor for Cu^{2+} spins, which decreases monotonically with increasing L, the polarization factor, and the interplane correlation function denoted by a solid line in Fig. 4(d) [Fig. 4(e)] is in accordance with the in-plane (out-of-plane) polarization of the $S_{\mathrm{tot},z} = \pm 1$ ($S_{\mathrm{tot},z} = 0$) mode. Ferromagnetic interplane correlations are indicated by positive α [$\alpha = 0.31(15)$]. The polarization analysis for the excitations around 5 meV close to the zone boundary, which is not shown, reveals mixing of the in-plane and out-of plane polarizations, or in other words the $S_{\mathrm{tot},z} = 0$ and $S_{\mathrm{tot},z} = \pm 1$ modes merge near the zone boundary.

C. Continuum scattering

The magnetic excitation spectrum between 2 and 7 meV in $Rb_2Cu_3SnF_{12}$ is markedly different from the spin-wave excitations observed in the classical spin-$\frac{5}{2}$ kagome lattice antiferromagnet $KFe_3(OH)_6(SO_4)_2$ (jarosite), which orders magnetically at low temperatures [41]. It also differs from the continuum of spinon excitations in herbertsmithite, where the ground state is believed to be a quantum spin liquid [29]. Resonant modes in $Rb_2Cu_3SnF_{12}$ [Fig. 5(a)] are found only around the zone center and their intensity decreases precipitously away from $(-2,0)$, while in jarosite the "weather-vane" mode exists throughout the Brillouin zone and in herbertsmithite the spinon continuum gives rise to hexagonal rings of diffuse scattering, surrounding zone centers [29]. However, between 8 and 10 meV we observe for $Rb_2Cu_3SnF_{12}$ weak diffuse scattering near $(-1.5,0)$ and $(-2.5,0)$ [Figs. 2(b), 2(d), and 5(b)] on both sides of the zone center $(-2,0)$, as in herbertsmithite. This scattering, which is diffuse in energy and broad in momentum, is different from the resolution-limited excitations below 8 meV and cannot be accounted for within the dimer series expansion. For herbertsmithite, the recent neutron scattering places an upper bound of 0.25 meV on any gap in the continuum of scattering [29]. On the contrary, the continuum in $Rb_2Cu_3SnF_{12}$ is observed well above the sharp dispersive modes of the pinwheel VBS state. Thus, while pinwheel dimerization and DM interactions in $Rb_2Cu_3SnF_{12}$ induce resonant modes at low energies, it appears that a threshold in energy exists beyond which a spin flip is no longer

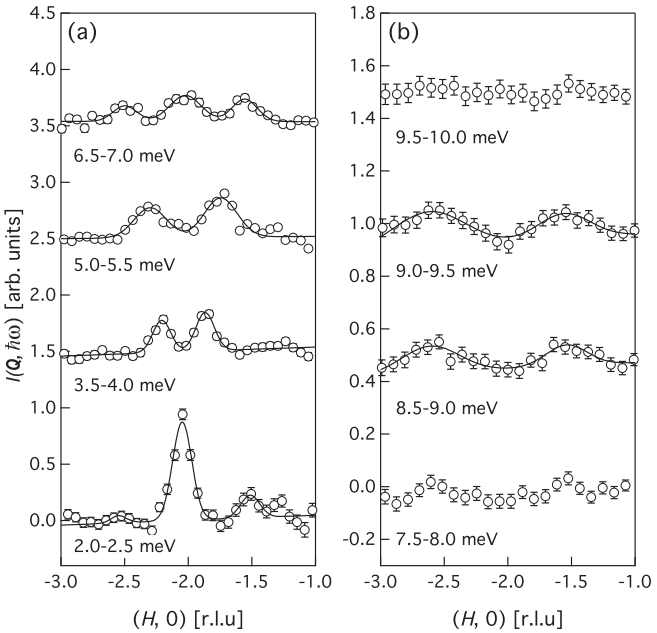

FIG. 5. Constant-energy cuts of $I(\mathbf{Q},\hbar\omega)$ are plotted as a function of H. The energy range of the integration is indicated below each data set. The intensity is averaged over the whole range of L and $\Delta\mathbf{Q}_{[-1,2]}$ of 0.045 Å^{-1}. The lines serve as guides to the eye. Data sets for different energy ranges in panels (a) and (b) are shifted vertically by 1 (1.5 for 2.0 to 2.5 meV) and 0.5, respectively.

a stable quasiparticle and the underlying quantum kagome nature of the material is apparent. Whether this scattering is best interpreted as resulting from two-magnon processes or magnon fractionalization will require a more detailed comparison between theories incorporating such features [42] and higher-quality scattering data.

IV. SUMMARY

High-intensity high-resolution pulsed neutron scattering unveils new features of the magnetic excitations in the pinwheel VBS state of the distorted kagome lattice antiferromagnet $Rb_2Cu_3SnF_{12}$. We observe a weakly dispersive mode around 5 meV and ghost modes, both of which are attributed to the enlarged unit cell caused by the structural transition at $T = 215$ K. Excitations below 8 meV appear to be well described by the dimer series expansion for the enlarged unit cell. The polarization analysis of the dominant modes is consistent with a splitting of the triplet into a $S_{\mathrm{tot},z} = 0$ singlet and a $S_{\mathrm{tot},z} = \pm 1$ doublet due to DM interactions. Between 8 and 10 meV, we observe continuum scattering, which is reminiscent of the fractionalized excitations recently observed in herbertsmithite.

ACKNOWLEDGMENTS

The work was supported in part by the Thailand Research Fund under Grant No. MRG55800, a Grant-in-Aid for Scientific Research from JPS (Grants No. 23244072, No. 24740223, and No. 23540395) and a Global COE Program funded by MEXT Japan. Work at the Institute for Quantum Matter was supported by the US Department of Energy, Office of Basic Energy Sciences, Division of Materials Sciences and Engineering under Award DE-FG02-08ER46544. The research at Oak Ridge National Laboratory's Spallation Neutron Source was sponsored by the Scientific User Facilities Division, Office of Basic Energy Sciences, U.S. Department of Energy.

[1] I. Syozi, Prog. Theor. Phys. **6**, 306 (1951).
[2] A. P. Ramirez, *Handbook of Magnetic Materials*, edited by K. H. J. Buschow (Elsevier Science, Amsterdam, 2001), Vol. 13, pp. 423–520.
[3] M. B. Hastings, Phys. Rev. B **63**, 014413 (2000).
[4] Y. Ran, M. Hermele, P. A. Lee, and X.-G. Wen, Phys. Rev. Lett. **98**, 117205 (2007).
[5] Y. Iqbal, F. Becca, S. Sorella, and D. Poilblanc, Phys. Rev. B **87**, 060405 (2013).
[6] Y. Iqbal, F. Becca, and D. Poilblanc, New J. Phys. **14**, 115031 (2012).
[7] S. Sachdev, Phys. Rev. B **45**, 12377 (1992).
[8] C. Waldtmann, H. U. Everts, B. Bernu, C. Lhuillier, P. Sindzingre, P. Lecheminant, and L. Pierre, Eur. Phys. J. B **2**, 501 (1998).
[9] C. Zeng and V. Elser, Phys. Rev. B **51**, 8318 (1995).
[10] G. Misguich, D. Serban, and V. Pasquier, Phys. Rev. Lett. **89**, 137202 (2002).
[11] S. Depenbrock, I. P. McCulloch, and U. Schollwöck, Phys. Rev. Lett. **109**, 067201 (2012).
[12] J. B. Marston and C. Zeng, J. Appl. Phys. **69**, 5962 (1991).
[13] P. Nikolic and T. Senthil, Phys. Rev. B **68**, 214415 (2003).
[14] R. R. P. Singh and D. A. Huse, Phys. Rev. B **76**, 180407(R) (2007).
[15] R. R. P. Singh and D. A. Huse, Phys. Rev. B **77**, 144415 (2008).
[16] B.-J. Yang, Y. B. Kim, J. Yu, and K. Park, Phys. Rev. B **77**, 224424 (2008).
[17] S. Yan, D. A. Huse, and S. R. White, Science **332**, 1173 (2011).
[18] J. S. Helton, K. Matan, M. P. Shores, E. A. Nytko, B. M. Bartlett, Y. Yoshida, Y. Takano, A. Suslov, Y. Qiu, J. H. Chung *et al.*, Phys. Rev. Lett. **98**, 107204 (2007).
[19] J. S. Helton, K. Matan, M. P. Shores, E. A. Nytko, B. M. Bartlett, Y. Qiu, D. G. Nocera, and Y. S. Lee, Phys. Rev. Lett. **104**, 147201 (2010).
[20] S.-H. Lee, H. Kikuchi, Y. Qiu, B. Lake, Q. Huang, K. Habicht, and K. Kiefer, Nat. Mater. **6**, 853 (2007).
[21] T.-H. Han, S. Chu, and Y. S. Lee, Phys. Rev. Lett. **108**, 157202 (2012).
[22] T.-H. Han, J. S. Helton, S. Chu, A. Prodi, D. K. Singh, C. Mazzoli, P. Muller, D. G. Nocera, and Y. S. Lee, Phys. Rev. B **83**, 100402 (2011).
[23] O. Ofer and A. Keren, Phys. Rev. B **79**, 134424 (2009).

[24] P. Mendels, F. Bert, M. A. deVries, A. Olariu, A. Harrison, F. Duc, J. C. Trombe, J. S. Lord, A. Amato, and C. Baines, Phys. Rev. Lett. **98**, 077204 (2007).
[25] F. Bert, D. Bono, P. Mendels, F. Ladieu, F. Duc, J. C. Trombe, and P. Millet, Phys. Rev. Lett. **95**, 087203 (2005).
[26] H. Yoshida, Y. Okamoto, T. Tayama, T. Sakakibara, M. Tokunaga, A. Matsuo, Y. Narumi, K. Kindo, M. Yoshida, M. Takigawa *et al.*, J. Phys. Soc. Jpn. **78**, 043704 (2009).
[27] G. J. Nilsen, F. C. Coomer, M. A. de Vries, J. R. Stewart, P. P. Deen, A. Harrison, and H. M. Rønnow, Phys. Rev. B **84**, 172401 (2011).
[28] B. Fåk, E. Kermarrec, L. Messio, B. Bernu, C. Lhuillier, F. Bert, P. Mendels, B. Koteswararao, F. Bouquet, J. Ollivier *et al.*, Phys. Rev. Lett. **109**, 037208 (2012).
[29] T.-H. Han, J. S. Helton, S. Chu, D. G. Nocera, J. A. Rodriguez-Rivera, C. Broholm, and Y. S. Lee, Nature (London) **492**, 406 (2012).
[30] K. Matan, T. Ono, Y. Fukumoto, T. J. Sato, J. Yamaura, M. Yano, K. Morita, and H. Tanaka, Nat. Phys. **6**, 865 (2010).
[31] E. Khatami, R. R. P. Singh, and M. Rigol, Phys. Rev. B **84**, 224411 (2011).
[32] T. Ono, K. Morita, M. Yano, H. Tanaka, K. Fujii, H. Uekusa, Y. Narumi, and K. Kindo, Phys. Rev. B **79**, 174407 (2009).
[33] K. Morita, M. Yano, T. Ono, H. Tanaka, K. Fujii, H. Uekusa, Y. Narumi, and K. Kindo, J. Phys. Soc. Jpn. **77**, 043707 (2008).
[34] G. Ehlers, A. A. Podlesnyak, J. L. Niedziela, E. B. Iverson, and P. E. Sokol, Rev. Sci. Instrum. **82**, 085108 (2011).
[35] R. T. Azuah, L. R. Kneller, Y. Qiu, P. L. W. Tregenna-Piggott, C. M. Brown, and J. R. D. Copley, J. Res. Natl. Inst. Stand. Technol. **114**, 341 (2009).
[36] K. Hwang, K. Park, and Y. B. Kim, Phys. Rev. B **86**, 214407 (2012).
[37] J. Oitmaa, C. Hamer, and W. Zhang, *Series Expansion Methods for Strongly Interacting Lattice Models* (Cambridge University Press, Cambridge, 2006).
[38] M. S. Grbić, S. Krämer, C. Berthier, F. Trousselet, O. Cepas, H. Tanaka, and M. Horvatic, Phys. Rev. Lett. **110**, 247203 (2013).
[39] Y. Nambu *et al.* (unpublished).
[40] S. W. Lovesey, *Theory of Neutron Scattering From Condensed Matter, Volume 2: Polarization Effects and Magnetic Scattering* (Clarendon Press, Oxford, 1984).
[41] K. Matan, D. Grohol, D. G. Nocera, T. Yildirim, A. B. Harris, S.-H. Lee, S. E. Nagler, and Y. S. Lee, Phys. Rev. Lett. **96**, 247201 (2006).
[42] M. Mourigal, W. T. Fuhrman, A. L. Chernyshev, and M. E. Zhitomirsky, Phys. Rev. B **88**, 094407 (2013).

http://dx.doi.org/10.7566/JPSJ.83.043701

Large Negative Quantum Renormalization of Excitation Energies in the Spin-1/2 Kagome Lattice Antiferromagnet $Cs_2Cu_3SnF_{12}$

Toshio Ono[1], Kittiwit Matan[2,3], Yusuke Nambu[4], Taku J. Sato[4], Kazuya Katayama[5], Satoshi Hirata[5], and Hidekazu Tanaka[5]

[1]*Department of Physical Science, School of Science, Osaka Prefecture University, Sakai 599-8531, Japan*
[2]*Department of Physics, Faculty of Science, Mahidol University, Bangkok 10400, Thailand*
[3]*ThEP, Commission of Higher Education, Bangkok 10400, Thailand*
[4]*Institute of Multidisciplinary Research for Advanced Materials, Tohoku University, Sendai 980-8577, Japan*
[5]*Department of Physics, Tokyo Institute of Technology, Meguro, Tokyo 152-8551, Japan*

(Received November 19, 2013; accepted February 14, 2014; published online March 5, 2014)

Magnetic excitations in the spin-1/2 distorted kagome lattice antiferromagnet $Cs_2Cu_3SnF_{12}$, which has an ordered ground state owing to the strong Dzyaloshinskii–Moriya interaction, were studied using inelastic neutron scattering. Although the spin-wave dispersion can be qualitatively understood in terms of linear spin-wave theory (LSWT), the excitation energies are renormalized by a factor of approximately 0.6 from those calculated by LSWT, almost irrespective of the momentum transfer. This inadequacy of LSWT, which is attributed to quantum fluctuations, provides evidence of negative quantum renormalization in the spin-1/2 kagome lattice antiferromagnet.

Ubiquitous magnetic excitations in conventional magnets with the Néel state are generally well described by LSWT. In low-dimensional quantum magnets, however, dominant quantum effects significantly modify the magnetic excitations. In particular, for an $S = 1/2$ antiferromagnetic Heisenberg spin chain, the exact spinon excitation energies are larger than that calculated using LSWT by a factor of $\pi/2$,[1)] which was verified through an inelastic neutron scattering experiment on the spin-1/2 one-dimensional (1D) Heisenberg antiferromagnet $CuCl_2{\cdot}2N(C_5D_5)$.[2)] This quantum enhancement of excitation energies is known as the quantum renormalization.

The spin-1/2 2D kagome-lattice antiferromagnet (KLAF) is a research frontier with the potential to realize a disordered ground state arising from the synergistic effect of strong frustration and quantum fluctuations.[3–13)] The theoretical consensus for the case of Heisenberg spins is that the classical Néel state, which is robust in conventional magnets, is supplanted by a disordered quantum state. However, the nature of the ground state, which is the basis for the discussion of excitations, has not been theoretically elucidated. Innovative theoretical studies have been conducted on the spin-1/2 nearest-neighbor Heisenberg KLAF using a variety of approaches. Most of the recent results suggest the existence of nonmagnetic ground states described by spin liquids[6–10)] and valence-bond solids.[11–13)] Experimentally, the lack of an ideal model has hindered detailed studies of intrinsic excitations of kagome magnets. Nevertheless, great effort has been made to search for approximate realizations of the spin-1/2 KLAF, which exhibits a diversity of states.[14–22)]

$A_2Cu_3SnF_{12}$ (A = Rb, Cs) is a promising family of spin-1/2 KLAFs.[20,21)] $Rb_2Cu_3SnF_{12}$ has a distorted kagome lattice and a gapped $S = 0$ singlet ground state.[20–22)] A study of singlet-to-triplet excitations in $Rb_2Cu_3SnF_{12}$ using inelastic neutron scattering revealed a pinwheel motif of strongly interacting dimers.[21–23)] All relevant spin Hamiltonian parameters were determined, which suggested the dominant effect of the Dzyaloshinskii–Moriya (DM) interaction.[21–24)] On the other hand, $Cs_2Cu_3SnF_{12}$ has a uniform kagome lattice at room temperature with the lattice parameters $a = 7.142(4)$ Å and $c = 20.381(14)$ Å,[20)] as shown in Fig. 1(a). This compound undergoes a structural transition at $T_s = 185$ K and magnetic ordering at $T_N = 20.0$ K.[20)] The magnetic susceptibility exhibits a small anomaly at T_s and a large increase at T_N [Fig. 2(a)]. The presence of superlattice reflections below T_s suggests the doubling of the in-plane lattice parameter, giving rise to a $2a \times 2a$ enlarged unit cell. Above T_N, the magnetic susceptibility is in good agreement with the theoretical susceptibility obtained from exact diagonalization for the 24-site kagome cluster[25)] [Fig. 2(a)]. This suggests that the exchange network remains approximately uniform.

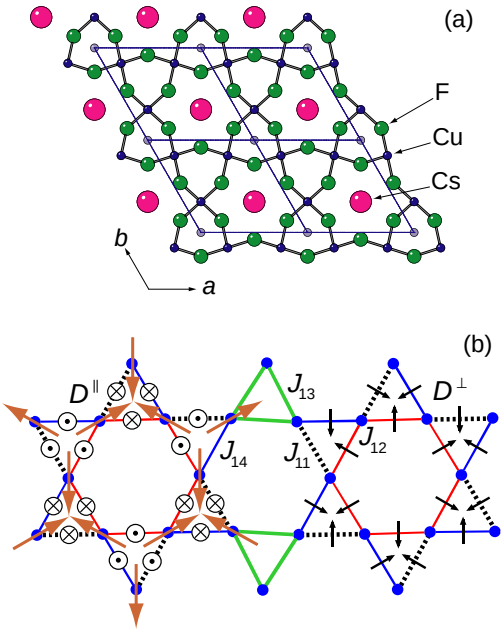

Fig. 1. (Color online) (a) Crystal structure at room temperature viewed along the *c*-axis, where fluorine ions located outside the kagome layer are omitted. Thin lines denote the unit cell. (b) Diagram showing the connectivity of $S = 1/2$ Cu^{2+} spins via the nearest-neighbor exchange interactions J_{11}, J_{12}, J_{13}, and J_{14}. Configurations of the out-of-plane component $D^{\parallel}$ and in-plane component $D^{\perp}$ of the DM vectors, deduced from the highly symmetric room-temperature structure, are illustrated on the left and right, respectively. The large arrows on the left indicate the $\boldsymbol{q} = 0$ structure assumed in the LSWT calculations.

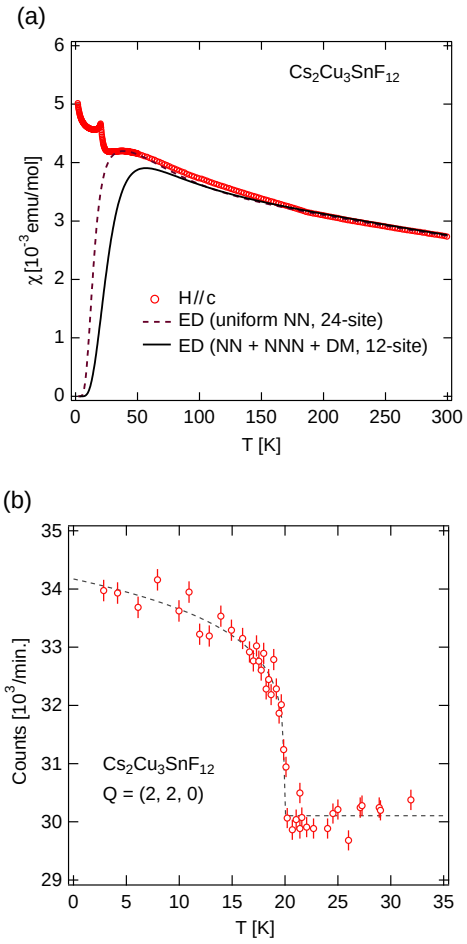

Fig. 2. (Color online) (a) Temperature dependence of magnetic susceptibility in $Cs_2Cu_3SnF_{12}$. Dashed line denotes the result obtained by exact diagonalization for a 24-site uniform kagome cluster with $J = 20.7$ meV and $g = 2.49$, while solid line is the result obtained for a 12-site distorted kagome cluster with $J_{\rm avg} = 19.8$ meV and the same interaction coefficients a_i, J_2/J_1 and d_z as those obtained from the analysis of spin-wave dispersions with $d_{\rm p} = 0$ and $g = 2.43$. (b) Temperature dependence of the magnetic Bragg reflection at $\boldsymbol{Q} = (2, 2, 0)$. The dashed line serves as a visual guide.

Low-energy magnetic excitations in the spin-1/2 distorted KLAF $Cs_2Cu_3SnF_{12}$ can be described by the collective disturbance of the ordered moments. Although these magnetic excitations in the classical spin-5/2 KLAF $KFe_3(OH)_6(SO_4)_2$ are well described by LSWT,[26,27] little is known about the quantum effect for the spin-1/2 case, where large quantum renormalization is expected to emerge. In this letter, we present the first evidence of the large negative renormalization of spin-wave energies with respect to the LSWT result in $Cs_2Cu_3SnF_{12}$. This observation provides a striking contrast to the well-known positive quantum renormalization of excitation energies in the $S = 1/2$ antiferromagnetic Heisenberg spin chain,[1] for which the renormalization factor is exactly $\pi/2$.

$Cs_2Cu_3SnF_{12}$ crystals were synthesized in accordance with the chemical reaction $2CsF + 3CuF_2 + SnF_4 \rightarrow Cs_2Cu_3SnF_{12}$. CsF, CuF_2, and SnF_4 were dehydrated by heating in vacuum at about 100 °C. First the materials were packed into a Pt tube of 9.6 mm inner diameter and 100 mm length in the ratio of 3 : 3 : 2. One end of the Pt tube was welded and the other end was tightly folded with pliers and placed between Nichrome plates. Single crystals were grown from the melt. The temperature of the furnace was lowered from 850 to 750 °C over 100 h. After collecting the well-formed pieces of crystal, we repeated the same procedure. Inelastic neutron scattering measurements were performed on two co-aligned single crystals of $Cs_2Cu_3SnF_{12}$ (total mass of 3.3 g) with a sample mosaic of about 1° at GPTAS and HER, which are triple-axis spectrometers run by the Institute for Solid State Physics, University of Tokyo. At GPTAS, the final energy of the thermal neutrons was fixed at 14.7 meV. The collimations were 40′–40′–sample–40′–80′. A pyrolytic graphite (PG) filter was placed after the sample to remove contamination from higher-order neutrons. The vertically focused (horizontally flat) PG crystals were used to analyze the scattered neutrons. At HER, the final energy of the cold neutrons was fixed at 5 meV. The scattered neutrons were analyzed using the central three blades of a seven-blade doubly focused PG analyzer. A cool Be or oriented-PG-crystal filter was placed in the incident beam and a room-temperature Be filter was placed in the scattered beam. In the analysis of the HER data, effective collimations of 10′–40′–sample–160′–120′ were used. For both experiments, the sample was aligned with the $(h, k, 0)$ plane horizontal to measure spin-wave excitations within the kagome plane. The sample was cooled to the base temperature of 3 K using a ^{4}He closed cycle cryostat.

Using the $2a \times 2a$ enlarged unit cell for the low-temperature crystal structure, we observed an increased scattering intensity due to magnetic Bragg reflections below $T_{\rm N} = 20.0$ K at $\boldsymbol{Q}_{\rm m} = (2m, 2n, 0)$, where m and n are integers. The ordering wave vectors correspond to the reciprocal lattice points of the uniform kagome lattice above $T_{\rm s} = 185$ K. Figure 2(b) shows the temperature dependence of the magnetic Bragg reflection at $\boldsymbol{Q} = (2, 2, 0)$. The scattering intensity above $T_{\rm N} = 20.0$ K arises from a nuclear reflection. This result indicates that the ordered state has a $\boldsymbol{q} = 0$ structure. Hence the center of the 2D Brillouin zone located at $\boldsymbol{Q}_{\rm m}$ is expected to give rise to strong spin-wave scattering.

Figure 3(a) shows constant-$\boldsymbol{Q}$ scans measured using the GPTAS spectrometer. The scans were performed at 3 K and at three different momentum transfers $\boldsymbol{Q} = (2, 2, 0)$, $(2.25, 2, 0)$, and $(2.267, 1.867, 0)$. At the zone center (Γ-point) $\boldsymbol{Q} = (2, 2, 0)$, we clearly observed two spin-wave excitations at 10.7(5) and 13.6(4) meV, and extra scattering above the background below 5 meV [top panel of Fig. 3(a)]. A high-resolution measurement using the cold-neutron spectrometer HER revealed a spin gap of 1.0(6) meV as shown in Fig. 3(c). Away from the zone center along the Γ → M and Γ → K directions, we clearly observed three peaks representing three branches of spin-wave excitations, as shown in the middle and bottom panels of Fig. 3(a), respectively. Figure 3(b) shows constant-energy scans taken along two independent high-symmetry directions from the Γ-point to the M- and K-points [Fig. 4(c)]. For both constant-$\boldsymbol{Q}$ and constant-energy scans, the peak width is resolution-limited and the line shape is well described by the convolution with the resolution function. As the temperature increases toward $T_{\rm N}$, the energy of the spin gap Δ, which scales with the order parameter, decreases toward zero and the peak width Γ, which is resolution-limited below 7 K, becomes broader, indicative of the shorter lifetime of the excitations, as shown in the inset

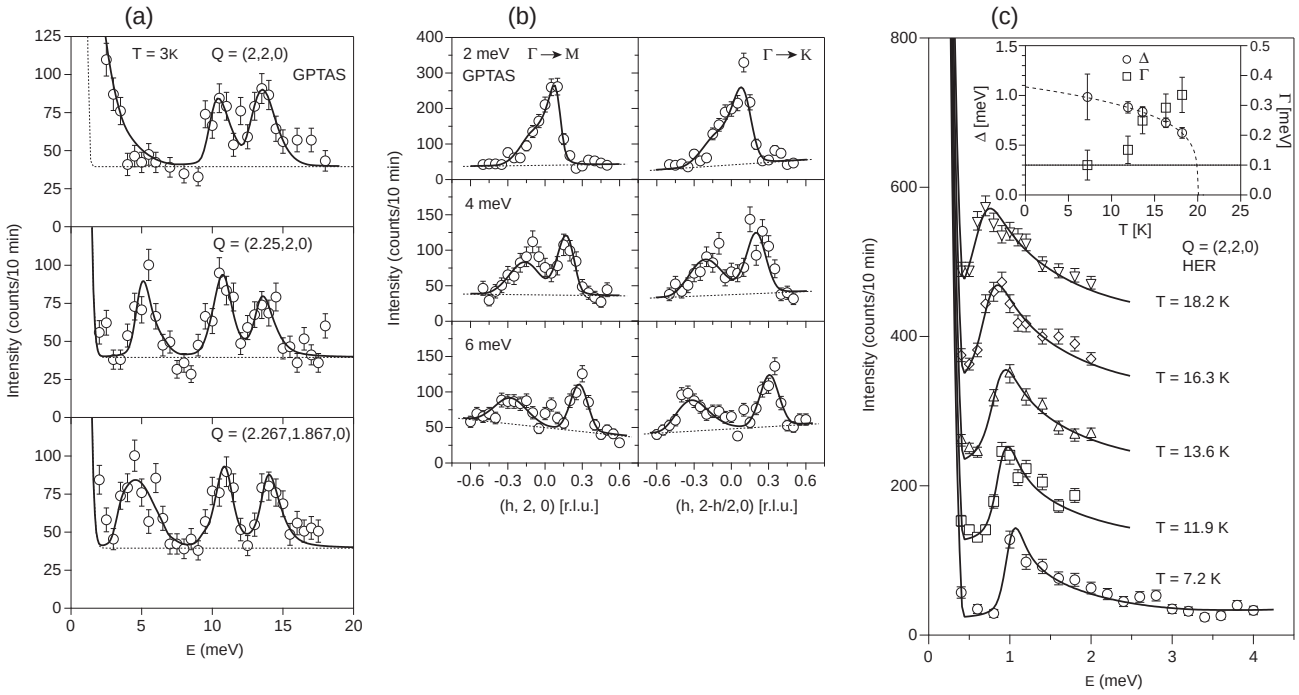

Fig. 3. (a) Constant-$\boldsymbol{Q}$ scans measured at $\boldsymbol{Q} = (2, 2, 0)$, $(2.25, 2, 0)$, and $(2.267, 1.867, 0)$. (b) Constant-energy scans measured at $\hbar\omega = 2$, 4, and 6 meV along two independent high-symmetry directions [see Fig. 4(c)]. (c) Temperature dependence of the spin gap at the Γ-point. The main panel shows constant-$\boldsymbol{Q}$ scans measured at the Γ-point at different temperatures. Data sets for different temperature are shifted vertically by 100. The inset shows the temperature dependences of the spin-gap energy Δ and peak width Γ. The dotted line denotes the resolution of the instrument obtained by the convolution fitting, and the dashed lines serve as a visual guide. The error bar denotes the statistical error.

of Fig. 3(c). Figures 4(a) and 4(b) show the spin-wave dispersions obtained from several constant-energy and constant-$\boldsymbol{Q}$ scans throughout the Brillouin zone along the two high-symmetry directions. The data points were obtained from resolution-convolution fits. Unfortunately, we were not able to determine the excitation energies of the high-energy modes owing to the high phonon background and low scattering intensity, which may be due to magnon instability.[28)]

We analyze the low-energy spin-wave dispersion observed in $Cs_2Cu_3SnF_{12}$ in the framework of LSWT. The underlying spin structure used to calculate the spin-wave dispersion is that of the $\boldsymbol{q} = 0$ structure for the uniform kagome lattice, in which all spins are oriented either toward or away from the center of a triangle [see Fig. 1(b)]. In our previous study on $Rb_2Cu_3SnF_{12}$ (Ref. 22), we found that the DM interactions play a dominant role in singlet–triplet excitations, i.e., a large out-of-plane component of the DM vectors gives rise to large splitting between the $S^z = \pm 1$ and 0 modes and reduces the energy gap at the Γ-point. Therefore, as a first approximation, we consider the DM interactions as the dominant anisotropy energy (referred to as the DM model), and express the spin Hamiltonian as

$$\mathcal{H} = \sum_{\langle i,j \rangle} \{J_{ij}(\boldsymbol{S}_i \cdot \boldsymbol{S}_j) + \boldsymbol{D}_{ij} \cdot [\boldsymbol{S}_i \times \boldsymbol{S}_j]\} + J_2 \sum_{\langle\langle k,l \rangle\rangle} (\boldsymbol{S}_k \cdot \boldsymbol{S}_l), \quad (1)$$

where J_{ij} and J_2 are the nearest-neighbor (NN) and next-nearest-neighbor (NNN) exchange interactions, respectively, and $\boldsymbol{D}_{ij}$ are DM vectors. J_{ij} are nonuniform as shown in Fig. 1(b), and their magnitude is scaled by J_1, which can be written as $J_{1i} = a_i J_1$ where $i = 1$, 2, 3, and 4, while the strength of the DM vectors $\boldsymbol{D}_{ij}$ is scaled by the corresponding exchange interactions, $D^{\parallel}_{ij} = d_z J_{ij}$ and $D^{\perp}_{ij} = d_p J_{ij}$, where the configurations of the out-of-plane ($D^{\parallel}_{ij}$) and in-plane ($D^{\perp}_{ij}$) components of the DM vectors are illustrated in Fig. 1(b). We neglect the interlayer interaction, because the triplet excitations in $Rb_2Cu_3SnF_{12}$ are dispersionless perpendicular to the kagome layer.[22)]

The LSWT calculations of the spin-wave dispersion as well as the scattering intensity for the DM model of Eq. (1), which are shown in Fig. 4(c) and Fig. S2 in Supplemental Materials,[29)] were performed using a symbolic algebra method written in Mathematica. Details of the LSWT calculations are described in Supplemental Materials.[29)] The results reveal 12 branches of spin-wave excitations, but only three dominant low-energy branches (Fig. S2) are observed experimentally. The strong inelastic scattering intensity centered around $\boldsymbol{Q}_m$ [Fig. 4(c)] is consistent with the experimental data. The obtained fit parameters are $J_1 = 13.6(3)$ meV, $a_1 = 1$ (fixed), $a_2 = 1.0(1)$, $a_3 = 0.84(7)$, $a_4 = 0.70(5)$, $J_2 = -1.07(2)$ meV, $d_z = -0.29(1)$ and $d_p = 0.057(4)$, giving $J^{sw}_{avg} = (J_{11} + J_{12} + J_{13} + J_{14})/4 = 12.1(7)$ meV. The solid lines in Figs. 4(a) and 4(b) represent the best fits with these parameters. The splitting of the two higher energy modes [ω_1 and ω_2, see Figs. 4(a) and 4(b)] at the Γ-point results from zone folding due to the structural transition. In the DM model, the energies of the ω_1 and ω_2 modes at the Γ-point are mainly determined by the out-of-plane component $D^{\parallel}$ of the DM vectors and the exchange interactions. The value of $D^{\parallel}$ is as large as $0.29J_{1i}$, which is the same order of magnitude as the value of $D^{\parallel}$ observed in $Rb_2Cu_3SnF_{12}$ (Ref. 22). This large out-of-plane component

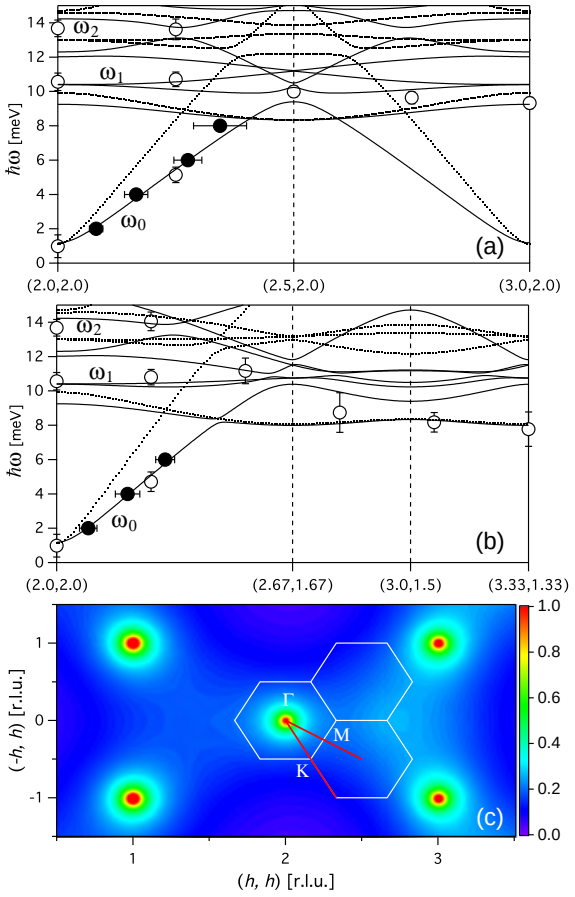

Fig. 4. (Color online) (a, b) Experimental data and calculated spin-wave dispersions along the two high-symmetry directions denoted by thick red lines in (c). Open symbols indicate the data measured around $(2, 2, 0)$ while closed symbols indicate the data measured at the equivalent point around $(0, 2, 0)$. Solid lines denote the best fit obtained using the DM model in Eq. (1), and dotted lines denote dispersions with $J_{\rm avg}^{\rm mag} = 19.8$ meV obtained from the magnetic susceptibility, $J_2 = -1.07$ meV, $d_z = -0.18$, and $d_{\rm p} = 0.033$. (c) Calculated energy-integrated scattering intensity of $Cs_2Cu_2SnF_{12}$.

of the DM vectors stabilizes the $\boldsymbol{q} = 0$ state, and thus is responsible for the magnetic ordering in $Cs_2Cu_3SnF_{12}$ as discussed by Cépas et al.[30] For a uniform kagome lattice, the in-plane component $D^{\perp}$ gives rise to the splitting of the ω_1 and ω_2 modes and the spin gap Δ, which are expressed as $\omega_2 - \omega_1 = (2D^{\perp}D^{\parallel})/(J_1 + J_2)$ and $\Delta = \sqrt{3}D^{\perp}$, respectively. The large splitting of the ω_1 and ω_2 modes and the small spin gap Δ cannot be consistently described by the DM model with uniform J_1, attesting to the necessity of a spin model with the enlarged unit cell and nonuniform J_{1i}. The ω_1 branch, which corresponds to the zero-energy mode in the absence of the DM interactions, is lifted considerably owing to the large $D^{\parallel}$. Its weak dispersion and lowest spin gap at the K-point can be ascribed to a small ferromagnetic next-nearest-neighbor interaction ($J_2 < 0$). Another possibility accounting for the dispersion of the ω_1 mode is the quantum fluctuations, which are dominant for the spin-1/2 case and favor the $\sqrt{3} \times \sqrt{3}$ ordering at the K-point over the $\boldsymbol{q} = 0$ ordering.[3,22,24]

Although the spin-wave dispersion observed in $Cs_2Cu_3SnF_{12}$ is qualitatively understandable in terms of LSWT and the DM model, there is a large quantitative disagreement between the exchange constant $J_{\rm avg}$ obtained from the spin-wave dispersion ($J_{\rm avg}^{\rm sw} = 12.1$ meV) and that obtained from the magnetic susceptibility data $J_{\rm avg}^{\rm mag}$. As shown by the solid line in Fig. 2(a), the magnetic susceptibility is best described using $J_{\rm avg}^{\rm mag} = 19.8$ meV when the interaction coefficients a_i, J_2/J_1 and d_z are fixed, as those obtained from the spin-wave data with $d_{\rm p} = 0$. Here, we neglected the small in-plane component of the DM vector $d_{\rm p}$. $J_{\rm avg}^{\rm mag} = 19.8$ meV should be close to the true exchange constant. However, the dotted lines in Figs. 4(a) and 4(b), which represent LSWT with $J_{\rm avg}^{\rm mag}$, show a large discrepancy between the LSWT result and the data especially for the ω_0 mode. We note that the slope of this mode is predominantly determined by $J_{\rm avg}$. Therefore, we deduce that the quantum fluctuations decrease excitation energies from those obtained by LSWT, i.e., negative quantum renormalization of the excitation energies occurs in $Cs_2Cu_3SnF_{12}$. For a spin-1/2 triangular-lattice Heisenberg antiferromagnet, a recent theory predicts that at high energies spin-waves are strongly renormalized, so that the dispersion becomes flat.[28,31,32] However, in contrast to the case of the triangular lattice, the renormalization factor ($R = J_{\rm avg}^{\rm sw}/J_{\rm avg}^{\rm mag} = 0.61$) in $Cs_2Cu_3SnF_{12}$ appears to be independent of the momentum transfer.

We note the renormalization factors in other low-dimensional antiferromagnets. For $Cu(DCOO)_2{\cdot}4D_2O$, which is described as an $S = 1/2$ square-lattice antiferromagnet, the positive quantum renormalization with $R = 1.21$ was reported.[33] This renormalization factor coincides with theoretical result.[34,35] For Cs_2CuCl_4, in which antiferromagnetic chains are coupled to form a spatially anisotropic triangular-lattice antiferromagnet, a large renormalization factor of $R = 1.63$ was reported.[36] This large positive quantum renormalization is attributed not to the triangular geometry of the lattice but to the spinon excitations characteristic of antiferromagnetic chain.[37] For $KFe_3(OH)_6(SO_4)_2$, which is described as an $S = 5/2$ uniform KLAF, the renormalization factor is estimated as $R = 0.90$ using the exchange constants determined from the dispersion relations[26] and magnetization and ESR measurements.[38] This fact together with the present result on $Cs_2Cu_3SnF_{12}$ shows that the negative quantum renormalization of the excitation energies is universal for KLAFs with an ordered ground state and enhanced with decreasing spin quantum number S.

Acknowledgments This work was supported by a Grant-in-Aid for Scientific Research from the Japan Society for the Promotion of Science, and the Global COE Program funded by the Ministry of Education, Culture, Sports, Science and Technology of Japan. H.T. was supported by a grant from the Mitsubishi Foundation. K.M. was supported by the Thailand Research Fund under grant No. MRG55800.

1) J. des Cloizeaux and J. J. Pearson, Phys. Rev. **128**, 2131 (1962).
2) Y. Endoh, G. Shirane, R. Birgeneau, P. Richards, and S. Holt, Phys. Rev. Lett. **32**, 170 (1974).
3) S. Sachdev, Phys. Rev. B **45**, 12377 (1992).
4) C. Waldtmann, H.-U. Everts, B. Bernu, C. Lhuillier, P. Sindzingre, P. Lecheminant, and L. Pierre, Eur. Phys. J. B **2**, 501 (1998).
5) H. Nakano and T. Sakai, J. Phys. Soc. Jpn. **80**, 053704 (2011).
6) F. Wang and A. Vishwanath, Phys. Rev. B **74**, 174423 (2006).
7) M. Hermele, Y. Ran, P. A. Lee, and X.-G. Wen, Phys. Rev. B **77**, 224413 (2008).
8) S. Yan, D. A. Huse, and S. R. White, Science **332**, 1173 (2011).
9) S. Depenbrock, I. P. McCulloch, and U. Schollwöck, Phys. Rev. Lett. **109**, 067201 (2012).
10) S. Nishimoto, N. Shibata, and C. Hotta, Nat. Commun. **4**, 2287 (2013).

11) R. R. P. Singh and D. A. Huse, Phys. Rev. B **77**, 144415 (2008).
12) G. Evenbly and G. Vidal, Phys. Rev. Lett. **104**, 187203 (2010).
13) K. Hwang, Y. B. Kim, J. Yu, and K. Park, Phys. Rev. B **84**, 205133 (2011).
14) M. P. Shores, E. A. Nytko, B. M. Bartlett, and D. G. Nocera, J. Am. Chem. Soc. **127**, 13462 (2005).
15) J. S. Helton, K. Matan, M. P. Shores, E. A. Nytko, B. M. Bartlett, Y. Yoshida, Y. Takano, A. Suslov, Y. Qiu, J.-H. Chung, D. G. Nocera, and Y. S. Lee, Phys. Rev. Lett. **98**, 107204 (2007).
16) T.-H. Han, J. S. Helton, S. Chu, D. G. Nocera, J. A. Rodriguez-Rivera, C. Broholm, and Y. S. Lee, Nature **492**, 406 (2012).
17) M. Müller and B. G. Müller, Z. Anorg. Allg. Chem. **621**, 993 (1995).
18) Z. Hiroi, M. Hanawa, N. Kobayashi, M. Nohara, H. Takagi, Y. Kato, and M. Takigawa, J. Phys. Soc. Jpn. **70**, 3377 (2001).
19) Y. Okamoto, H. Yoshida, and Z. Hiroi, J. Phys. Soc. Jpn. **78**, 033701 (2009).
20) T. Ono, K. Morita, M. Yano, H. Tanaka, K. Fujii, H. Uekusa, Y. Narumi, and K. Kindo, Phys. Rev. B **79**, 174407 (2009).
21) K. Morita, M. Yano, T. Ono, H. Tanaka, K. Fujii, H. Uekusa, Y. Narumi, and K. Kindo, J. Phys. Soc. Jpn. **77**, 043707 (2008).
22) K. Matan, T. Ono, Y. Fukumoto, T. J. Sato, J. Yamaura, M. Yano, K. Morita, and H. Tanaka, Nat. Phys. **6**, 865 (2010).
23) K. Matan, Y. Nambu, Y. Zhao, T. J. Sato, Y. Fukumoto, T. Ono, H. Tanaka, C. Broholm, A. Podlesnyak, and G. Ehlers, Phys. Rev. B **89**, 024414 (2014).
24) K. Hwang, K. Park, and Y. B. Kim, Phys. Rev. B **86**, 214407 (2012).
25) G. Misguich and P. Sindzingre, Eur. Phys. J. B **59**, 305 (2007).
26) K. Matan, D. Grohol, D. G. Nocera, T. Yildirim, A. B. Harris, S. H. Lee, S. E. Nagler, and Y. S. Lee, Phys. Rev. Lett. **96**, 247201 (2006).
27) T. Yildirim and A. B. Harris, Phys. Rev. B **73**, 214446 (2006).
28) A. L. Chernyshev and M. E. Zhitomirsky, Phys. Rev. B **79**, 144416 (2009).
29) (Supplemental Material) Details of the LSWT calculations of the spin-wave dispersion and the scattering intensity for the DM model of Eq. (1) are described in Supplemental Materials.
30) O. Cépas, C. M. Fong, P. W. Leung, and C. Lhuillier, Phys. Rev. B **78**, 140405(R) (2008).
31) O. A. Starykh, A. V. Chubukov, and A. G. Abanov, Phys. Rev. B **74**, 180403(R) (2006).
32) W. Zheng, J. O. Fjærestad, R. R. P. Singh, R. H. McKenzie, and R. Coldea, Phys. Rev. B **74**, 224420 (2006).
33) H. M. Rønnow, D. F. McMorrow, R. Coldea, A. Harrison, I. D. Youngson, T. G. Perring, G. Aeppli, O. Syljuåsen, K. Lefmann, and C. Rischel, Phys. Rev. Lett. **87**, 037202 (2001).
34) J. Igarashi, Phys. Rev. B **46**, 10763 (1992).
35) R. R. P. Singh and M. P. Gelfand, Phys. Rev. B **52**, R15695 (1995).
36) R. Coldea, D. A. Tennant, and Z. Tylczynski, Phys. Rev. B **68**, 134424 (2003).
37) M. Kohno, O. A. Starykh, and L. Balents, Nat. Phys. **3**, 790 (2007).
38) T. Fujita, H. Yamaguchi, S. Kimura, T. Kashiwagi, M. Hagiwara, K. Matan, D. Grohol, D. G. Nocera, and Y. S. Lee, Phys. Rev. B **85**, 094409 (2012).